

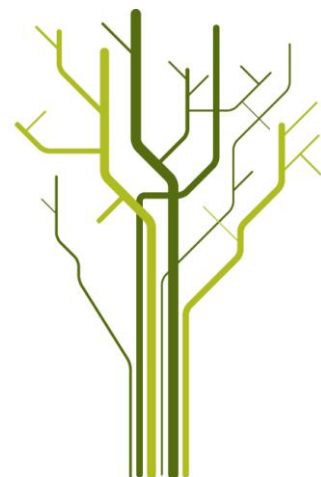
Comparing SAR measurements of natural oil seeps in the Gulf of Mexico with mineral and biological slicks in the North Sea



Claes Anders Storm Hanssen

FYS-3921 Master's Thesis in Electrical Engineering

June 2013



Abstract

In this thesis, natural oil seeps in Synthetic Aperture Radar (SAR) images are studied. The intension is to compare seeps to known oil slicks as emulsion-oil, crude-oil and plant-oil. TerraSAR-X and Radarsat-2 data with these different slicks are analyzed. Polarimetric features are extracted for all the scenes, histograms and scatterplots of values from the slicks are evaluated. Finally a classification is performed on images with slicks that are suspected to be seeps. Natural oil seeps are hydrocarbons seeping out of fissures at the bottom of the ocean. If they reach the surface, they form oil-slicks with different shapes. Seeps are one of the biggest sources of oil-pollution and make a big threat to the marine environment. SAR is one of the most used tools for detecting oil at the ocean surface. Oil in SAR-images appear as dark slicks because the oil is dampening the Bragg waves, makes the surface less rough which reduce the radar backscatter. A main task in oil detection is to distinguish between real oil slicks and other phenomena that can cause dark patches in a SAR-image. One way to do this is to look at multi-polarization features and see how the patches behave. The features extracted in this thesis seems to separate oil from the sea really good. It looks like the *entropy* and the *mean radar backscatter* are the best features. Visually, the seeps have quite similar values as the emulsion and crude oil. Inspection of the scatterplots and histograms from the features show that the seeps have slightly different values from the crude-oil. An attempt to classify the potential seeps from the dataset as either crude-oil or plant-oil is performed by the use of a maximum likelihood classification based on the polarimetric features. The classification states that the dark patches from the Gulf are most probably crude-oil rather than plant-oil.

Acknowledgements

First of all, I want to thank my supervisor Camilla Brekke for all her help, advice and sharing of knowledge. She has followed up my progress from the beginning to the end and I have learnt a lot from our discussions. I am very grateful for all the time she has spent on reading my thesis and providing all the feedback I have received.

Thanks to Stine Skrunes for her advice and help in all the issues I have faced during my programming.

I would also like to thank Kongsberg Satellite Services for the great possibility of using all the satellite images used in this thesis.

Thanks to the organization On Wings of Care for giving valuable photos of natural seeps.

Finally, I want to thank all my friends and my girlfriend for all the support and encouragement they have given me to write this thesis.

Contents

1	Introduction	9
1.1	Motivation	9
1.2	Main objectives of this thesis	10
1.3	Main contribution to the field	10
1.4	Structure of the thesis	11
2	Remote sensing with Synthetic Aperture Radar	13
2.1	SAR techniques and imaging geometry	13
2.2	Polarization of SAR	15
2.3	Different polarization channel systems	16
2.4	Multi-polarization features	17
2.5	SAR image properties	17
2.6	Polarimetric SAR Systems	18
2.6.1	Environmental satellite (Envisat)	18
2.6.2	TerraSAR-X	18
2.6.3	COSMO-SkyMED	18
2.6.4	Radarsat-2	18
3	SAR measurements of dark slicks	21
3.1	Oil-slicks characteristics	21
3.2	Mineral slicks, biogenic slicks and other slick look-alikes	22
3.3	Weathering processes	23
3.3.1	Evaporation	23
3.3.2	Emulsification	23
3.3.3	Dispersion	23
4	General concepts of natural oil seeps	25
4.1	Characteristics of natural seeps	25
4.2	Displacement of a seep	25
4.3	Weathering of seeps from the seafloor	25
4.4	Previous studies on SAR and natural oil seeps	26
5	Data set and study areas	29
5.1	Study sites	29
5.1.1	Gulf of Mexico	29
5.1.2	The North sea	29
5.1.3	Ground truth and auxiliary data	29

6	Methodology	35
6.1	Eigenvector-eigenvalue decomposition	35
6.1.1	Entropy H	36
6.1.2	Mean scattering angle $\bar{\alpha}$	36
6.1.3	Anisotropy A	36
6.2	Polarimetric features from the covariance matrix	36
6.2.1	Mean radar backscatter μ	36
6.2.2	Co-polarization ratio γ_{co}	37
6.2.3	Standard deviation (std) of the co-polarized phase difference (CPD)	37
6.2.4	Correlation magnitude ρ_{co}	37
6.2.5	Real part of the co-polarization correlation r_{co}	37
6.3	Statistical methods and preprocessing	37
6.4	Classification	38
6.4.1	Segmentation of the dark spots	38
6.4.2	Supervised maximum likelihood classification	38
6.5	Signal to noise analysis	41
7	Results and discussion	43
7.1	Presentation of the values from the polarimetric features	43
7.2	Results of the scatterplots	45
7.2.1	Entropy vs. mean radar backscatter	46
7.2.2	Anisotropy vs. mean radar backscatter	46
7.2.3	Real part of the co-polarization correlation vs. mean radar backscatter	46
7.2.4	Real part of the co-polarization correlation vs. correlation magnitude	46
7.3	Results of Histograms	47
7.3.1	Histograms of H	47
7.3.2	Histograms of μ	47
7.3.3	Histograms of r_{co}	47
7.3.4	Histograms of ρ_{co}	47
7.3.5	Histograms of γ_{co}	47
7.4	Results of signal-to-noise analysis	47
7.5	Classification results	48
7.6	Discussion of the scenes	48
8	Conclusion	67
8.1	Future work	67

Chapter 1

Introduction

1.1 Motivation

Oil spills are a major threat to the marine environment and may have huge consequences for the wildlife, fisheries and human health. They are caused by spills from oilrigs, leaking pipelines, deliberate discharges from boats and seepages by natural causes. Synthetic Aperture Radar (SAR) has in past studies proven to be the most useful tool in monitoring these spills due to its all-day and all-weather capabilities. Oil on the ocean reduces the roughness of the surface due to the dampening of capillary waves and lower dielectric constant than water, which results in less radar backscattering than the sea surrounding the oil [1]. Therefore oil spills appear as dark spots in SAR-images. Nevertheless, other natural phenomena can also create dark spots in SAR images, they are termed oil slick *look-alikes* and may include natural films, low wind, heavy rain, grease ice etc. [2]. A main task in oil spill monitoring is to distinguish real oil spills from these look-alikes.

Natural oil seeps are oil drops and bubbles flowing up from fissures at the bottom of the ocean. Some parts of these oil and gas bubbles reach the surface and form a thin layer at the top [3]. In 2003 a global-estimate of all the oil that entered the marine environment stated that 47% was from natural seeps and 53% from leaks and human accidents [4]. With such a big part of all the oil, natural seeps may be the most important single source of oil pollution that enters the ocean. Known seeps are located in the Gulf of Mexico, the Caspian Sea, the Barents sea, the ocean outside California and Brazil, West Africa, and Indonesia [5]. Most of the already known seeps are located in the Gulf of Mexico (GoM) [6]. There are over 600 natural oil seeps that seep out around 500 000 to one million barrels of oil each year, that is approximately 4000 to 200 000 tons [4]. Remote sensing by the use of SAR to detect and localize these seeps has been of relevance due to the threat of pollution, but also a possible localization for oil-companies to drill.

A lot of studies of oil-pollution have been executed by the use of SAR-data. In 1987, Bartsch et al. [7] used an L-band (1-2 GHz) and an X-band (8-12 GHz) SAR to study the ability of SAR to detect, localize and discriminate oil pollutions with different characteristics. Several controlled and different slicks were released by ships. The sensors managed to both detect and localize the slicks, but failed to discriminate between them. In the early 90's, ERS-1 SAR images were used by a lot of researchers. Bjerde et al. [8] in 1993 used ERS-1 data to test an algorithm for segmentation of oil-slicks and look-alikes. The algorithm showed good results and was improved by more training data. Radarsat-1 was launched in 1995 and operated by the Canadian Space Agency and has provided good SAR-data for a lot of different purposes. Marghany [9] used Radarsat-1 data to monitor the movement and transportation of oil spills. Most of the satellites with a SAR-sensor in the 1980s and 1990s operated with a single-polarized system. As the years have passed, more satellites have been launched with different SAR polarization systems which have brought new and much more opportunities for researchers. European Space Agency's (ESA) Envisat Satellite ASAR data was used to characterize slicks from the Prestige tanker accident [10]. The quad-polarimetric system of Radarsat-2 have been used to distinguish oil spills from biogenic slicks [11].

To detect oil-spills and distinguish them from other look-alikes, different types of algorithms are used. Zhang et al. [12] used the co-occurrence matrix of SAR-images to extract textural features and identify oil spills from these. In 2007, Solberg et al. [13] used an algorithm that first detected dark spots, extracted features from these spots and classified them as either oil spills or look-alikes. Later, more advanced algorithms have been developed for detecting and classifying oil spills [14], [15], [16] and [17].

Lately, multi-polarization features have been used to distinguish oil-spills from look-alikes. The $H/A/\bar{\alpha}$ -decomposition have been performed on SAR-images and showed possibilities to separate oil-spills and biogenic slicks [11], [18], and [19]. In Skrunes et al. [20], eight different polarimetric features were used to discriminate between crude-oil, emulsion and plant-oil (look-alike). The result showed that the features managed to distinguish between the plant-oil and the crude-oil. This thesis explores the power of these multi-polarization SAR features in characterizing natural seeps, i.e. discriminate seeps from other marine slick types.

1.2 Main objectives of this thesis

In the summer of 2012, a dataset of seven different images from the GoM were obtained for a Multimission Oil Spill Detection (MOISD) project, lead by Kongsberg Satellite Services (KSAT). The dataset includes three fine quad-polarimetric Radarsat-2 images, two single polarization wide swath Radarsat-2 images and two dual-polarimetric images from TerraSAR-X and COSMO-SkyMed. Due to the lack of groundtruth from these scenes, there is no concrete information about what the images contains, but they are suspected to be seeps. Also during the writing of this thesis, two Radarsat-2 images were acquired, one containing a seep and sargassum confirmed by the environmental organisation On Wings Of Care. Sargassum is a sort of seagrass and can be considered as a look-alike. The main aim with this thesis is to study SAR's capability to study natural oil seeps and also explore the ability to discriminate between crude-oil, biogenic slicks and natural seeps with multipolarization features.

1.3 Main contribution to the field

During the oil-on-water (OPV) exercise by the Norwegian Clean Seas Association for Operating Companies (NOFO) in June 2011, three different types of oil were released in the North Sea, i.e. crude-oil, plant-oil and oil-emulsion. Two different data sets were obtained during this exercise, a quad-polarimetric Radarsat 2 image (OPV-scene) and a dual-polarimetric TerraSAR-X image, both containing all three slicks. Previous work on the dataset have recently been done by Skrunes et al. [20], [21] and [22] which included an investigation of the ability of Radarsat 2 and TerraSAR-X to detect oil spills. Also, characterization of the oil spills and discrimination between the slicks were done for both sensors. In this thesis the OPV-image have been used as a reference and the information found have been used to quantify what the images from the GoM contain. The polarimetric features from Skrunes et al. [21] have been extracted from all the GoM-scenes. Histograms and scattering plots of the features were inspected to see which features that gave best separability between oil, water and slick types. Values from the OPV scene in these features were used to see if they match values of the slicks from the GoM-scenes. Also, data from the OPV-scene have been used in a trained classification to classify the rest of the GoM-scenes. Visual observations from the polarimetric features showed that the seeps behave similar as the crude oil and also have similar properties. Further investigation from the scatterplots and histograms showed that the values from the seeps actually are slightly different. The classification performed based on the features states that the dark patches from the GoM-scenes are most similar to emulsion and crude-oil.

1.4 Structure of the thesis

The thesis consists of one theoretical part and one experimental part. The theoretical part will be covered in chapter 2, 3 and 4, the experimental part is covered in chapter 5, 6 and 7 .

In Chapter 2 a brief introduction to the SAR-sensor is given. The first section will cover the sensor and the imaging geometry, the second section explains the polarization of SAR and the third section gives an overview over different satellites that are loaded with a SAR-sensor.

Chapter 3 gives an introduction to oil-spill measuring. First part of the chapter explains how oil-slicks appear in a SAR image and how they look. Second part will give an overview of different look-alikes and the third part an overview of processes that affect the oil-slick appearance in a SAR image.

Chapter 4 covers the basics of natural oil seeps. In the first part, the physics behind seeps will be explained. In the second part a summary of previous study and research of seeps is given.

In Chapter 5 the dataset of this thesis is presented. First of all the study areas are covered, secondly some information is given about the scenes. Information includes ground truth and two tables of useful facts about the different scenes.

Polarimetric feature extraction and selection is covered in chapter 6. In the first part, an overview of all the results that will be produced are given. Second part includes a theoretical part about all the polarimetric features and a discussion. Also the results are presented in this chapter.

The last chapter, number eight, concludes the whole work.

Chapter 2

Remote sensing with Synthetic Aperture Radar

Radar is an active sensor that measures distances to other objects by transmitting electromagnetic waves to the targets, and then receive echoes reflected by the targets. A radar system operates in the microwave region (300 GHz to 300 MHz, 1 mm to 1 m, X-, C, L, P-band) and penetrates clouds, smoke, rain etc. Also, SAR has it's own illumination and is therefore independent of illumination from the Sun, so the SAR-sensor is both day-time and weather independent. One of the most important aspects with Synthetic Aperture Radar (SAR) is its high spatial resolution. The technique to achieve this is based on the fact that the target stays in the beam for an extended period of time, and it will be observed from a range of positions along the flight path. In the past years, several books have been written about the theory of SAR-imaging. This chapter will use [23] and [24] as references to explain SAR geometry and polarization (section 1 and 2) at a "need to know" level.

2.1 SAR techniques and imaging geometry

An imaging SAR system consists of three different parts: a transmitter to transmit the signal, a receiver for the backscattered signal and an antenna which is used for both the transmission and the reception. The system is mounted on an airborne/spaceborne platform. As seen from figure 2.1, SAR operates in a sidelooking geometry from the platform at an altitude H . The beam from the SAR is aimed perpendicular to the flight direction or the azimuth direction (y-direction in figure 2.1), with a look angle θ_0 . There are two other directions that have to be defined. The first one is the ground range which is the x -direction in figure 2.2, the second is the slant range r , which is the radar-line-of-sight. Pulses of electromagnetic waves are transmitted from the sensor and hit the surface of the Earth. The covered area by the beam is called the footprint of the antenna. The pulses are then backscattered from the surface and the receiver on the platform picks them up. All the signals are then synthesized to a 2-D high spatial resolution image [23].

The size of the antenna footprint (θ_X, θ_Y) is defined from the length and width of the antenna:

$$\theta_X \approx \frac{\lambda}{L_X} \quad \text{and} \quad \theta_Y \approx \frac{\lambda}{L_Y} \quad (2.1)$$

where L_X and L_Y are the length of the antenna in the ground and azimuth direction respectively. λ is the wavelength of the carrier frequency transmitted from the antenna. θ_X and θ_Y are illustrated in figure 2.2 and 2.3 [23]. The range swath and azimuth swath can be derived as:

$$\Delta X \approx \frac{R_0 \theta_X}{\cos \theta_0} \quad \text{and} \quad \Delta Y \approx R_0 \theta_Y \quad (2.2)$$

where R_0 is the distance from the antenna to the illuminated area.

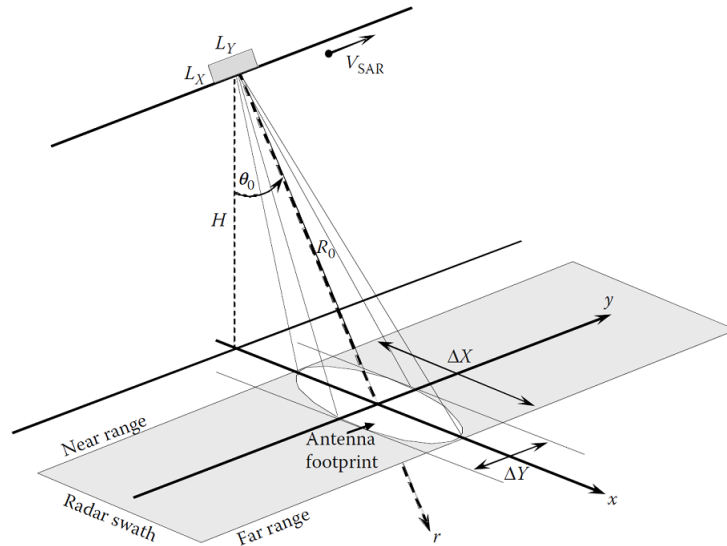


Figure 2.1: The geometry of SAR imaging from [23]

Spatial resolution: Spatial resolution describes the ability of the SAR to discriminate between two close targets. The spatial resolution of a SAR-image is really high taken to account the big altitude, up to 800 km. To achieve this, short pulses are needed. Also a good signal-to-noise ratio is preferred so high energy is also necessary. High energy and short pulses are usually very difficult to achieve and also expensive. For SAR this is solved by transmitting longer pulses where the energy is distributed over the time the pulses use. To keep the range resolution high by the use of short pulses, modulated pulses are transmitted by the use of "pulse-compression". This includes varying the frequency of the signal while the pulse is transmitted. Such a signal is called chirp and the frequency has a bandwidth B at the carrier frequency f_0 . At the end, a matched filter is used to compress the received pulse to achieve a good duration equal to $1/B$ [23].

In ground range the pulses are separated by the time delay between the received pulses. As seen from figure 2.2, the pulses have shorter pathway closer to the satellite in near range than far range. The resolution in ground range is given as:

$$\delta x = \frac{c}{2B \sin \theta} \quad (2.3)$$

where θ is the incidence angle illustrated in figure 2.2 and c is the speed of light.

In azimuth direction another technique has to be used to separate the pulses because, as seen from figure 2.3, the pulse will hit the surface at the same time and then received at the same time. A real aperture radar can only discriminate targets in azimuth direction if the distance between the targets is longer than the beamwidth [24]. The resolution for a real aperture radar is:

$$\delta y = \Delta Y = R_0 \theta_y = \frac{R_0 \lambda}{L_y} \quad (2.4)$$

So, to get a good resolution in azimuth direction with real aperture radar, a really long antenna is needed. To achieve high resolution, the concept "synthetic aperture" is used. This is making a long effective antenna by moving the the sensor in the azimuth direction. The length of the synthetic aperture is the flight path from

where a target comes into the footprint until the target is out of the footprint [24]. Azimuth resolution is given by:

$$\delta y = \frac{L_y}{2} \tag{2.5}$$

so the length of the antenna decides the resolution. Note that, the azimuth resolution is only dependent on the antenna length and hence independent of the distance to the ground.

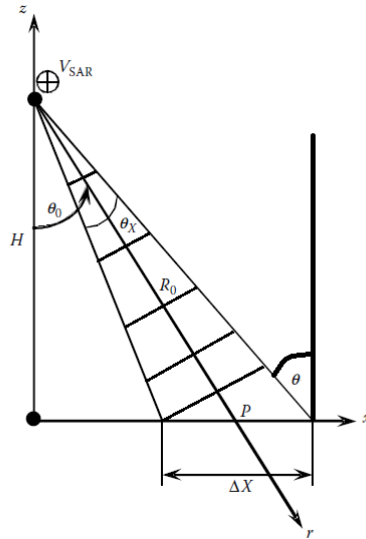


Figure 2.2: The geometry of SAR imaging in the altitude ground range domain from [23]

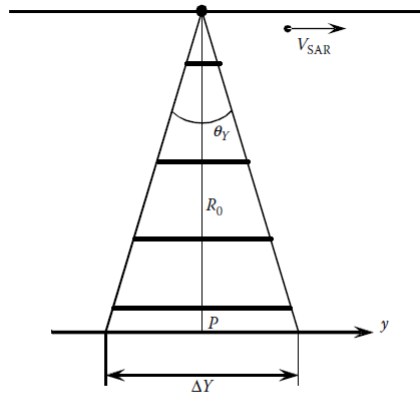


Figure 2.3: The geometry of SAR imaging in the slant range azimuth domain from [23]

2.2 Polarization of SAR

Electromagnetic waves consist of an electric and magnetic field, both perpendicular to each other in free space and transverse to the propagation direction. The polarization lies in the direction of the amplitude \mathbf{A} from the electric field [24] which is a two dimensional complex vector defined as:

$$\mathbf{A} = a_h e^{i\delta_h} \hat{\mathbf{h}} + a_v e^{i\delta_v} \hat{\mathbf{v}} \quad (2.6)$$

where $\hat{\mathbf{h}}$ is the basis vector for horizontal polarization and $\hat{\mathbf{v}}$ for the vertical, a_h and a_v the amplitudes and δ_h and δ_v the phases [24]. Polarization can be described as a shape on the background in space, from the tip of the electric field during the propagation. The points of this shape in the $\hat{\mathbf{h}} - \hat{\mathbf{v}}$ plane is $E_h = a_h \cos \delta_h$ and $E_v = a_v \cos \delta_v$. They also satisfy the expression of an ellipse:

$$\left(\frac{E_h}{a_h}\right)^2 + \left(\frac{E_v}{a_v}\right)^2 - 2\frac{E_h E_v}{a_h a_v} \cos(\delta_h - \delta_v) = \sin^2(\delta_h - \delta_v) \quad (2.7)$$

so electromagnetic waves are usually elliptically polarized. There are two cases where this changes. The first case is when $\delta_h - \delta_v = n\pi$, where n is an integer, there will be linear polarization. Secondly if $\delta_h - \delta_v = \pm\pi/2$ and the two amplitudes are equal, there will be a circular polarization. The electromagnetic waves transmitted from the SAR-system that acquired images for this thesis were linearly polarized.

When the electromagnetic waves are backscattered, the waves can be described by a new two dimensional complex vector. So scattering can be seen as an operator that makes a complex vector to another complex vector. This can be described by the complex scattering matrix \mathbf{S} :

$$\mathbf{E}^{sc} = \begin{bmatrix} S_{hh} & S_{hv} \\ S_{vh} & S_{vv} \end{bmatrix} \mathbf{E}^{tr} = \mathbf{S} \mathbf{E}^{tr} = e^{j\phi_{vv}} \begin{bmatrix} |S_{hh}| e^{j\phi_{co}} & |S_{hv}| e^{j\phi_{hv}} \\ |S_{vh}| e^{j\phi_{vh}} & |S_{vv}| \end{bmatrix} \quad (2.8)$$

Here \mathbf{E}^{tr} is the electric field transmitted from the satellite and \mathbf{E}^{sc} the received electrical field [24]. The elements in the \mathbf{S} -matrix are the complex scattering coefficients where the subindices denotes the transmitted and received polarization respectively. $\phi_{co} = \phi_{hh} - \phi_{vv}$ is the co-polarized phase difference (CPD).

The voltage that the radar measures is given by:

$$V = \mathbf{p}^{rec} [\mathbf{S}] \mathbf{p}^{tr} \quad (2.9)$$

where \mathbf{p}^{tr} is the normalized polarization vector which describes the transmitting radar antenna, \mathbf{p}^{rec} describes the receiving. With the voltage, we can also derive the power received by the radar which is simply magnitude of the voltage squared:

$$P = VV^* = |\mathbf{p}^{rec} [\mathbf{S}] \mathbf{p}^{tr}|^2 = (\overline{\mathbf{A}} \mathbf{l}) (\mathbf{l} \mathbf{A})^* = \overline{\mathbf{A}} \mathbf{l}^* \mathbf{A}^* = \mathbf{A} [\mathbf{C}] \mathbf{A}^* \quad (2.10)$$

Here $\overline{\mathbf{A}} = (p_h^{rec} p_h^{tr} \quad p_h^{rec} p_v^{tr} \quad p_v^{rec} p_h^{tr} \quad p_v^{rec} p_v^{tr})$ is transpose of the polarization vector elements, \mathbf{l} the Lexicographic scattering vector and \mathbf{C} is the covariance matrix [24].

2.3 Different polarization channel systems

The simplest channel system of SAR is the single-polarization (single-pol) SAR system. It uses a single linear polarization by transmitting and receiving horizontal or vertical polarized pulses. The first SAR systems that were made were usually operating with a single channel system. Dual polarization (dual-pol) SAR systems provide data from two channels, (HH, VV), (HH, HV) or (VH, VV). Most of the SAR data that are collected are from these kind of system and many satellites, like TerraSAR-X and COSMO-SkyMED, use dual-pol. Full polarimetric or quad-pol systems transmit and receive the signal in both direction (HH, HV, VH, VV). Only this system achieves the full scattering matrix \mathbf{S} and gives the opportunity of polarimetric feature extraction

that includes the cross-pol channels. One disadvantage with quad-pol is the smaller antenna footprint than the other systems [25].

Studies have been made to compare the performance in different areas between the systems. Lee et al. [26] compared the classification of crop and trees capability between the systems, and the quad-pol system proved to give the best results. Preferred polarization depends on the frequency of the radar and the wind speed of the scene. Studies state that there is no difference in using the HH or VV channel in oil spill detection, except for C-band where the VV channel seems to be the best, when strong wind is present [27].

2.4 Multi-polarization features

In section 2.2, the Lexicographic scattering vector was introduced. With the assumption of reciprocity, $S_{vh} = S_{hv}$, the Lexicographic vector and the Pauli vector $\underline{\mathbf{k}}$ are extracted from the \mathbf{S} -matrix as follow [23]:

$$\underline{\mathbf{l}} = [S_{hh} \sqrt{2}S_{hv} S_{vv}]^T \quad (2.11)$$

$$\underline{\mathbf{k}} = \frac{1}{\sqrt{2}}[S_{hh} + S_{vv} \ S_{hh} - S_{vv} \ 2S_{hv}]^T \quad (2.12)$$

where T denotes the transposed. The covariance matrix \mathbf{C} and the coherency matrix \mathbf{T} are respectively derived from the Lexicographic vector and the Pauli vector as:

$$[\mathbf{C}] = \frac{1}{L} \sum_{i=1}^L \underline{\mathbf{l}}_i \underline{\mathbf{l}}_i^{*T} \quad (2.13)$$

$$[\mathbf{T}] = \frac{1}{L} \sum_{i=1}^L \underline{\mathbf{k}}_i \underline{\mathbf{k}}_i^{*T} \quad (2.14)$$

where L is the number of pixels of the average window (in this thesis $9 \times 9 = 81$) and $*T$ is the complex conjugate and transpose. In Skrunes et al. [21] a signal to noise comparison was made and they concluded that the cross-polarization channels contained too much noise and therefore they are excluded from this thesis. So, the Lexicographic scattering vector is reduced to $\underline{\mathbf{l}} = [S_{hh} \ S_{vv}]^T$ and the covariance matrix becomes:

$$[\mathbf{C}] = \begin{bmatrix} \langle |S_{hh}|^2 \rangle & \langle S_{hh} S_{vv}^* \rangle \\ \langle S_{vv} S_{hh}^* \rangle & \langle |S_{vv}|^2 \rangle \end{bmatrix} \quad (2.15)$$

where $\langle \rangle$ denotes the average [20]. The Pauli vector for dual-polarizations $\underline{\mathbf{k}} = \frac{1}{\sqrt{2}}[S_{hh} + S_{vv} \ S_{hh} - S_{vv}]$, and the coherency matrix $[\mathbf{T}]$ are given as:

$$[\mathbf{T}] = \begin{bmatrix} \langle |S_{hh} + S_{vv}|^2 \rangle & \langle (S_{hh} + S_{vv})(S_{hh} - S_{vv})^* \rangle \\ \langle (S_{hh} - S_{vv})(S_{hh} + S_{vv})^* \rangle & \langle |S_{hh} - S_{vv}|^2 \rangle \end{bmatrix} \quad (2.16)$$

2.5 SAR image properties

The images that are processed in this thesis are generated from the \mathbf{S} -matrix. As mentioned in section 2.2.1, the coefficients of the \mathbf{S} -matrix are complex and they represent a look. The SAR can split the full aperture into smaller subapertures by splitting the bandwidth to sub-bands. Each of these subbands represent a single look of the scene and also one coefficient of the \mathbf{S} -matrix. So data that includes the \mathbf{S} -matrix is therefore called single-look-complex (SLC) data [28]. With a first look at a SAR-image, one of the first things to notice is a pattern of dots with different brightnesses. This phenomenon is called speckle noise and is caused by random interference of many coherent wave components backscattered from many different targets in the illuminated area [29]. Speckle is unwanted in the image because it can cover different targets and also make the interpretation of the

image more difficult. A lot of studies have been made in the past to develop algorithms that can reduce the speckle noise or even remove it [30],[31] and [32]. The most common solution is to use a certain amount of the single looks, sum them together and take the average to get a multilook image. This is an averaging method called multilooking and is done by deriving the mean value of a group of neighbor pixels. Multilook reduce the speckle noise, but will also smooth the image so some information will be lost. In this thesis, all the images are multilooked with a 9×9 window.

2.6 Polarimetric SAR Systems

2.6.1 Environmental satellite (Envisat)

Envisat was launched into orbit 1 March 2002 to an altitude of 790 km. This Earth-observation satellite was operated by the European Space Agency (ESA) until April 2012 when they lost contact with it, but it is still orbiting the Earth [33]. Envisat carried a lot of different remote-sensing instruments, including Advanced Synthetic Aperture Radar (ASAR). Operated at C-band (5.33 GHz), the Envisat provided images either with dual-pol or single pol. Envisat made measures of the atmosphere, ocean, forests and sea ice. A lot of research have been done from Envisat-data like [13], [17], [34] and [35].

2.6.2 TerraSAR-X

TerraSAR-X is a German satellite launched into space June 2007. It provides high resolution radar images, operating with an X-band (9.6 GHz) at an altitude of 514 km in a polar orbit [36]. TerraSAR-X have different operation modes which provides different resolution:

- Spotlight mode, gives a 10×10 km scene with a resolution of 1-2 m
- Stripmap mode, gives strips up to 30 km with a resolution of 3-6 m
- ScanSAR mode, gives strips up to 100 km with a resolution of 16 m

The SAR system gives single-pol or dual-pol data for scientific research [23]. X-band is more sensitive to damping of Bragg waves than C-band, but usually X-band has a higher noise floor which can cause the signal to be more corrupted with noise and limit the abilities to detect for example oil.

2.6.3 COSMO-SkyMED

COSMO-SkyMED (Constellation of small Satellites for the Mediterranean basin Observation) is an Italian system of four satellites operated by the Italian Space Agency. The first one was launched 8 June 2007, while the last one was launched 5 November 2010. They have a so called Ping-Pong mode and operate with an X-band. The Ping-Pong mode has a time lag between the H- and V-channel transmission which can make images over sea surfaces more fuzzy [37]. However, a new generation of COSMO-SkyMED satellites are planned to be launched which will cooperate with the first ones and strengthen their current capability. They will also have operational quad-polarimetric mode.

2.6.4 Radarsat-2

Radarsat-2 was launched 14 December 2007 and is controlled by the Canadian Space Agency (CSA). The satellite has a C-band SAR and operates with a quad-pol system at an altitude of 798 km. The antenna is 15 meter long and 1.5 meter wide and provides images with resolution up to 3 meters, depending on which mode that is used. See figure 2.4 for an illustration of the different beam modes. Radarsat-2's fully polarimetric datasets have improved the ability to characterize physical properties of objects and retrieve biological or geophysical properties from surface of the Earth [38]. Five of the images processed in this thesis are from this sensor.

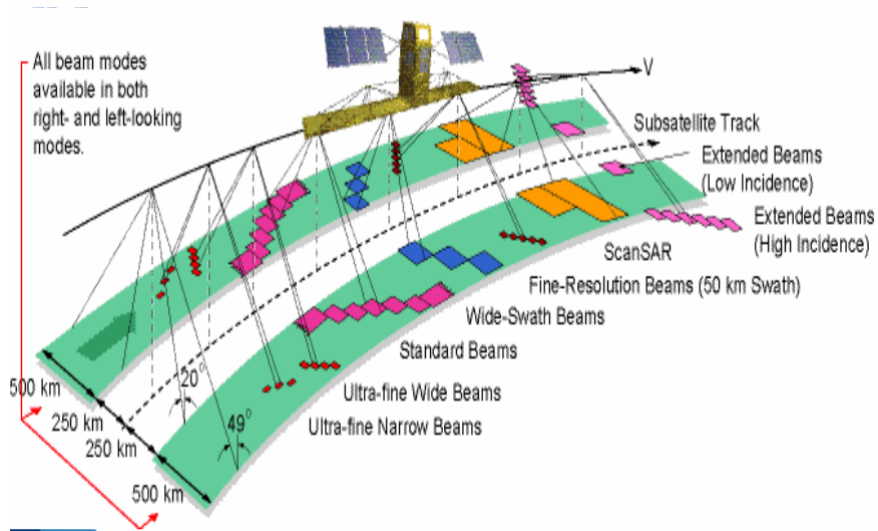


Figure 2.4: All the beam modes of Radarsat-2 from [38]

Chapter 3

SAR measurements of dark slicks

One of the more essential applications for SAR is to detect and monitor oil spills and locate different sources of oil pollution in the sea. Sources to oil spills can be oilrigs, leaking pipes, oil from ship accidents and illegal discharges. When a potential spill in a SAR image is detected, manual inspection of the slick is performed and also planes or helicopter can be sent to confirm if it is a spill or not. If the slick is pollution, aid is sent to prevent the pollution from growing and reduce the damages. An introduction to how oil-slicks are detected is given in this chapter. A list of different types of slicks and look-alikes are given and a brief introduction to different weathering processes that can affect oil-slicks.

3.1 Oil-slicks characteristics

Radar frequency bands have wavelengths from approximately 2.3 cm (X-band) up to 1 meter (P-band). Some of the roughness on the ocean surface is capillary and small gravity waves (5-10 cm) created by wind. The electromagnetic waves transmitted from the SAR sensor are, based on the Bragg model, in resonance with the waves [39]. The SAR-sensor is therefore sensitive to ocean surface short-waves also known as "Bragg-waves". These waves are dampened by the presence of oil and oil-slicks, which will cause a smoother surface than the surroundings and reduce the radar backscatter. Oil will therefore appear as dark spots in a SAR-image [40]. This is well described with both theory and experiments in [41], [42], [43] and [44]. The shape of an oil-slick depends on many factors like the oil type, the source of the pollution (moving or nonmoving) and how much oil the slick consists of [45]. Also weather conditions like wind speed and wind direction will affect the appearance of an oil slick since the slick will move with the waves which are strongly dependent on the wind. Knowledge about the wind speed is important because if the wind is too high, the waves will be too long and the surface will be too rough to be dampened by the oil. If the wind speed is too low, the ocean will be too smooth and appear dark in the SAR-image as well. A normal threshold for the wind speed for oil detection is around 3 m/s up to 10 m/s [46].

Minchew et al. [1] state that another source that reduce the radar backscatter is the change in dielectric constant or complex permittivity ϵ_c . The dielectric constant is an indicator of how a medium reacts to an electric field. The complex permittivity is given as:

$$\epsilon_c = \epsilon' - j\epsilon'' \quad (3.1)$$

where ϵ' is the real part which is the dielectric constant and describes a mediums ability to store electromagnetic energy. ϵ'' is the imaginary part and called the loss factor and describes how much energy the medium will lose and $j = \sqrt{-1}$. The SAR beam penetrates the medium it hit's on the ocean surface with a few millimeters. How much the beam penetrates a medium is decided by the dielectric constant of the certain medium. Whether the medium is a good conductor or a bad conductor is described by the loss tangent, $\tan\delta = \epsilon''/\epsilon'$. If the tangent is much higher than 1 it's a good conductor, if the tangent is much lower than 1 the medium is a bad conductor. A good conductor will give lower radar backscatter than a bad conductor because of the penetration

that occurs for a low loss medium most of the times leads to an increased volume scattering [47]. Oil has a dielectric constant with real part between 2.2 and 2.3, an imaginary part less than 0.02 while water has a real part greater than 60 and an imaginary part higher than 40 [1]. So water is a better conductor than oil thereby the definition of the loss tangent.

The reflection of a SAR-wave is a function of the incidence angle θ . There are two different ocean backscattering mechanisms, depending on θ . The first one is the Kirchoff's scattering when $\theta \in [0^\circ, 15^\circ]$ and the second one is the Bragg reflection when $\theta \in [20^\circ, 70^\circ]$ [27]. Bragg reflection allows the observation of Bragg waves which is dampened by oil slicks. When the incidence angle is increased the radar backscatter is decreased [48] and may limit the detection of oil slicks. The ideal incidence angle for oil slick monitoring is $\theta \in [20^\circ, 45^\circ]$ [27].

3.2 Mineral slicks, biogenic slicks and other slick look-alikes

Mineral slicks are usually made by discharges from boats and accidents. Brekke et al. [49] describes some different mineral slicks:

- *Oil-spills* caused by accidents or illegal disposal of oil products. Technical problems and mistakes can cause oil-spills from vessels and rigs.
- *Polluted water from rigs* is cleansed before it's released into the ocean, but always contains some oil and chemical byproducts that can damp the Bragg waves.
- *Liquid drilling fluid* which is used when a rig is drilling for oil. After a couple of uses, the fluid is then remade back to what it was, but the water from this process is released into the ocean which can form dark spots in the SAR-image.

Natural phenomena can also appear as dark patches in SAR-images due to different reasons. They are called oil-spill look-alikes and in the following are some of them presented:

- *Biogenic slicks or natural films* which are plankton, plants and materials from fish released into the ocean. These substances accumulate at the ocean surface due to their chemical properties. At the surface they are quickly dispersed and disappear depending on the wind conditions. The higher wind speed, the less probability to observe biogenic slicks because higher waves remove the films from the surface by wave breaking [47], [49].
- *Low wind areas*, as mentioned in section 3.1, appear dark in the SAR-image. This is because the wind is generating Bragg waves and when the wind is too low ($\text{wind} < 3\text{m/s}$), there will be no Bragg waves and the area will appear as a dark spot.
- *Rain cells* can cause low backscatter in a SAR-image in two ways. First of all attenuation in the atmosphere from volume scattering will decrease the backscattering where it's raining. Secondly, rain drops can also dampen the Bragg waves on the ocean surface, this depends on the wave height, wind speed and rain rate [47], [49].
- *Internal gravity waves* can influence the speed of the ocean waves and therefore cause change in the Bragg waves. They appear as parallel dark and light bands in the SAR-image and usually occur where the ocean is not so deep [49].

All these phenomenons are dependent of either wind, location or what kind of weather it is. Information about these factors can help to understand what a SAR-image contains.

3.3 Weathering processes

This section will present some weathering processes and how they affect oil in the sea. As soon as the oil has entered the marine environment, weathering processes will immediately start to change the physical and chemical properties of the oil-slick. All these changes determine how detectable and measurable the oil-spill is in a SAR-image [45].

3.3.1 Evaporation

At the ocean surface, evaporation is one of the most crucial processes causing the reduction in mass. After a few days at the surface, the oil has lost some of its original mass depending on the density of the oil. Light crude oil can lose up to 75%, medium crude oil lose up to 40% while heavy crude oil only lose up to 10% [50]. Even though evaporation is an important process, the knowledge of it is poor due to the complexity of the physics and chemistry behind this process. Most work has been to establish equations that quote how much mass the oil spill have lost. Fingas [51] stated that there are only two important factors in oil-evaporation, time t and temperature T and the evaporation percentage P can be expressed as:

$$P = C(T) \ln(t) \quad (3.2)$$

where C is a constant depending on temperature and can be derived from distillation data [50]. So more and more oil will evaporate while the time is passing, and the oil-slick will be more difficult to detect in a SAR-image.

3.3.2 Emulsification

Emulsification is the process when the water is mixed with the oil, it is called a water-in-oil emulsion. This can either happen at the ocean surface, but also for a natural seep that is moving up towards the surface. Emulsion changes the physical properties of the original oil in many ways. The density of the oil can be increased also the viscosity can be increased which will again cause slower evaporation [45].

3.3.3 Dispersion

Dispersion is the process when the hydrocarbons are spreading over a larger area. As soon as the oil is added to the surface, the oil will start to disperse and will continue until the whole slick is gone either by evaporation or sinking [50]. The dispersion is decided by the amount of oil in the slick and the wind because the dispersion is increased by larger ocean waves [52].

Chapter 4

General concepts of natural oil seeps

Seepages of natural causes are one of many the dark-slicks that can be observed in a SAR-image. Seeps start at the bottom of the ocean and have to go through a lot of processes that can change some properties and locations of the seep. This chapter gives an introduction to what natural seeps are and different processes that affect seeps. Also a brief overview of previous work on seeps by the use of SAR is given.

4.1 Characteristics of natural seeps

Natural seeps are hydrocarbons seeping out of faults at the bottom of the sea. They are transported in migration pathways up to the surface where they form a slick [53], see figure 4.1 which shows a seep from the Gulf of Mexico. A natural seep occurs when the seafloor that confines the oil is breached. This happens due to overpressure and buoyancy force becomes larger than the capillary resistance that kept the oil confined. Depending on the level of overpressure, there can be two types of seep. If the overpressure is moderate and breaches the seal, the seep will be widespread but will have a low intensity and stops when the openings are locked. If the overpressure is growing large enough to break the rock's minimum stress, the rock will fracture, form a fissure and there will be a high intensity seep [54]. Natural seepages form different shapes at the top of the surface like small spots, loops, hooks and circles, all affected by wind and currents. Usually natural seeps are thinner than mineral oil which can make them harder to detect [55]. At the surface, all the weathering processes introduced in section 3.3 will start to affect and decide the shape and the time the slick will exist.

4.2 Displacement of a seep

When the seep has reached the surface, it is usually located a couple of hundred meters away from the seep source. The location is a function of the rise speed, estimated by previous study to approximately 20 cm/s [5], currents beneath the sea and distance from the source to the surface [5]. The longer path the seep has to reach the surface, the further away it ends up from the source. Higher rise speed will reduce the distance to the location. In many cases, several different seeps can be observed in the same area. This does not necessarily mean that there are as many seep sources because some of them may be from the same one. A seep source can create several slicks by either various activity and separation during the rise process [5].

4.3 Weathering of seeps from the seafloor

A study by Leifer and Macdonald [56] suggest that the oil from seeps are mainly transported to the surface by gas bubbles. The oil lies as a thin layer outside the bubbles when they are rising upwards from the seafloor. Before a seep reaches the surface, there are different processes that can affect the seep. These processes reduce the amount of bubbles of the seep and affect the size, thickness and chemical properties of the seep at the surface. Here are some of the different processes:



Figure 4.1: A photo of a natural seep in the Gulf of Mexico in image #4. Copyright OnWingsOfCare.org

- *Dissolution* is the process when the oil makes a solution with the water. This happens mostly from the seafloor up to the surface, but can also occur at the top of the surface. The loss of oil in this process is not so big, but the loss of gas bubbles is big because gas has higher solubility than oil. Over 90% of the gas bubbles are dissolved beneath the sea surface which limits the chances of gas bubbles covered with oil to reach the surface [57], [58].
- *Oxidation* is the process when the hydrocarbons are oxidized to other chemical compositions like alcohols. How much the hydrocarbons are oxidized depends on the size of the hydrocarbon molecules, amount of oxygen available, temperature and energy from the Sun [50].
- *Emulsification*, as mentioned in section 3. 3. 2, occur at the top of the surface for oil spills, but for a seep it starts beneath the surface. This can slow and also eventually stop the seep from reaching the surface.

4.4 Previous studies on SAR and natural oil seeps

During the past years, several studies of seeps by SAR have been executed. Most of the studies have been in the Gulf of Mexico due to the high hydrocarbon seep activity.

Garcia-Pineda et al. [3] processed a dataset of more than 700 Radarsat-1 images from the Gulf. A texture-classifying neural network algorithm was used for classification between seeps and look-alikes which showed an accuracy of 98.22% and 97.74% for two test sets [59].

A lot of focus has been directed to the southern part of the Gulf to monitor the Cantarell seep. Rodriguez et al. [60] made an impact model of the Cantarell natural seep with SAR-data and wind information. Other studies from the Cantarell complex can be found in [61], [62], [63].

Thankappan et al. [64] reported a study using single-polarised TerraSAR-X data to investigate its capability to detect oil seeps. To use multi-polarization in seep studies have been suggested [62] and [64], but few have

been conducted [5]. This thesis take it to the level of using both dual-pol X-band and quad-pol C-band with TerraSAR-X and Radarsat-2 respectively, to study seeps.

Chapter 5

Data set and study areas

The dataset used in this thesis consists of six SAR-images. Five of them are quad-pol images from Radarsat-2 and the last one is a dual-pol image from TerraSAR-X. All these images contain different dark-slicks of interest. Ground truth information, weather data and study areas are presented in this chapter.

5.1 Study sites

This thesis has two different study areas. The first place is the Gulf of Mexico where all the seeps studied in this thesis are localized. The second place is the North Sea where the slicks that will be used as a basis are located.

5.1.1 Gulf of Mexico

The main part of the study areas for this thesis is three different locations in the Gulf of Mexico. The first place is the Cantarell Complex which is an oil field first discovered by a fisherman named Cantarell in 1976. The second one is to the south-west of Mississippi river in the northern part of the Gulf while the third is to the south east of the same river. See figure 5.1 and 5.2 for map and location of the SAR-images. For image #4 in figure 5.3 two points in the area are marked as sargassum and natural seep, both were observed and photographed by the wildlife and ecosystem protecting organization On Wings Of Care 02/04-2013. This happened in cooperation between JPL and University of Tromso to gather SAR-data and airplane photos simultaneously.

5.1.2 The North sea

The Norwegian Clean Seas Association for operating Companies (NOFO) made their oil-on-water exercise in the North Sea in June 2011. Controlled oil slicks were released into the ocean which gave an excellent opportunity for satellites to acquire images of the place with different slicks and ground truth information about them [21]. The oil slicks were crude oil, emulsion and plant oil which were all caught on the same scene by both TerraSAR-X and Radarsat-2, see figure 5.3 for the location. Previous work from these scenes can be found in Skrunes et al. [21] and [22].

5.1.3 Ground truth and auxiliary data

Kongsberg Satellite Service (KSAT) has provided all the images for this thesis. Some of the images are too big to be run in Matlab, so smaller parts of them are taken out. See figure 5.4 for the selected sub-regions that will be processed and what they contain. See Table 5.1 for more information about the images and Table 5.2 for another overview of what the images contain. The modes in Table 5.1 are FQ which denotes Fine Quad-polarimetric and SM that denotes Stripmap.

Image	OPV	#1	#2	#3	#4	#5
Day	8/6-11	14/8-11	14/8-11	27/8-11	4/4-13	17/7-12
Time	17:27	11:57	11:57	12:19	00:06	00:12
Sensor	RS2	RS2	RS2	RS2	RS2	TSX
Mode	FQ	FQ	FQ	FQ	FQ	SM
Polarization	Quad	Quad	Quad	Quad	Quad	HH VV
Wind Speed (m/s)	1-3	3.7	3.7	1.7	7.72	4.4
Incidence angle (deg)	34.49:36.1	46.8:48.02	46.8:48.02	22.24:24.16	46.8:47.99	37.08:38.42

Table 5.1: Information for all the scenes.

Image	OPV	#1	#2	#3	#4	#5
Oil-slick type	Crude-oil, emulsion and plant oil	Potential seep	Potential seep	Potential seep	Seep and sargassum	Cantarell seep

Table 5.2: Overview of what the scenes contains.

As weather data, the wind speed was needed as explained in section 3.1. The only problem here was the Meteorological Institute did not have access to weather data from the Gulf of Mexico, so the wind speed in Table 5.1 are downloaded from weather stations [65] close to the locations of the images in figure 5.1-5.3. As seen from the values, almost all the wind speeds are within the threshold of 3-10 m/s except the wind speed in image #3. For this image the wind speed is 1.7 m/s which can bring dark spots from low wind effect which have to be taken into account during the data analysis. As seen from figure 5.4 (f) there are some dark places which can be low wind areas. Another thing to point out is the grayscale image of image #4 in figure 5.4 (e). The seep and sargassum are brighter than the ocean, which indicate that ocean is smoother than the slicks. This creates some doubt about the information of the image received is correct.



Figure 5.1: The two first sites of the Gulf of Mexico study area. The locations where the images were acquired.

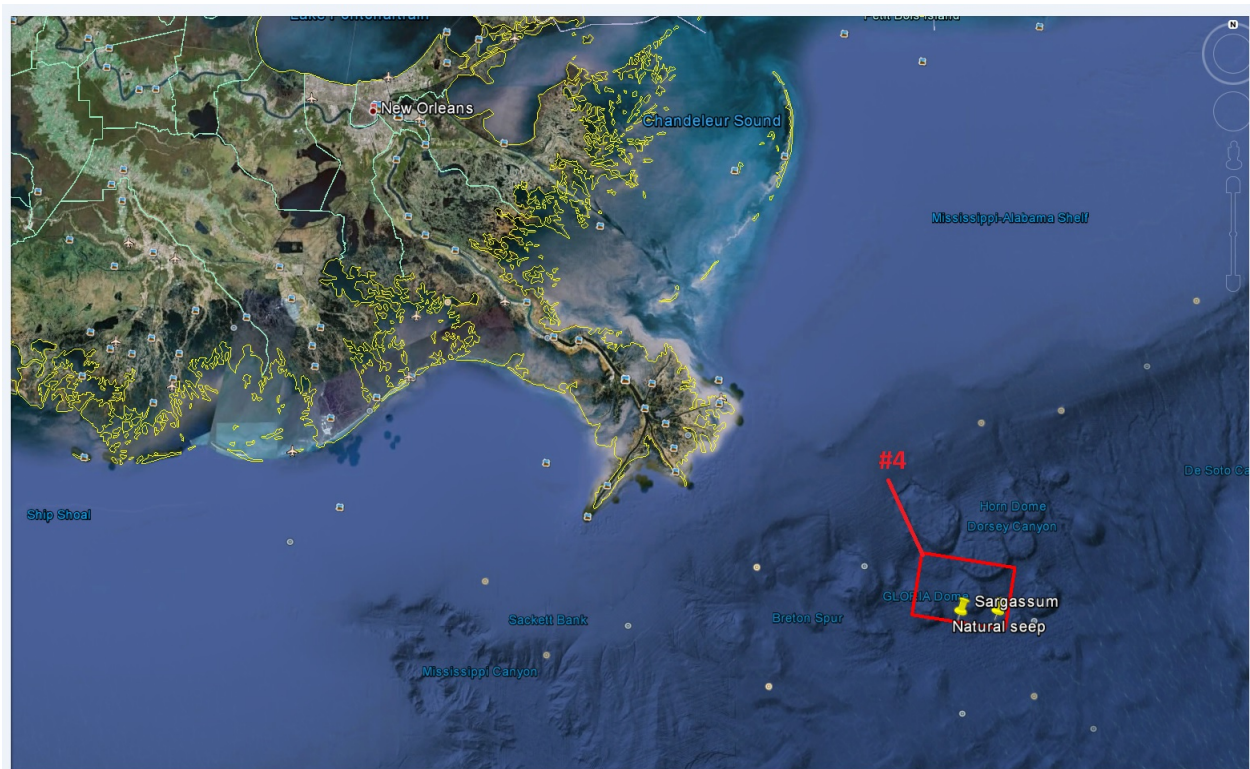
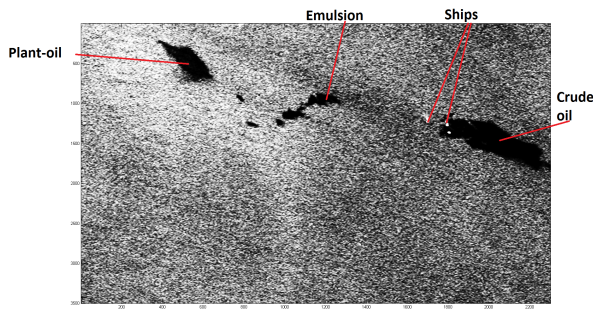


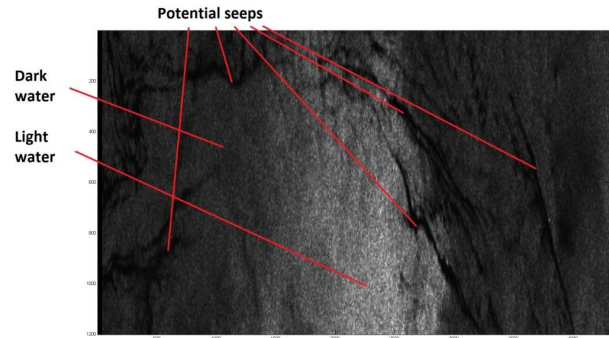
Figure 5.2: Third and last part from the Gulf of Mexico study area. Sargassum the point to the left and the seep the point to the right.



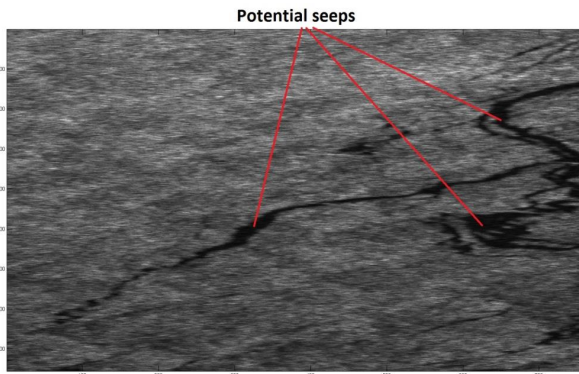
Figure 5.3: The OPV-scene in the North Sea between Norway and Scotland.



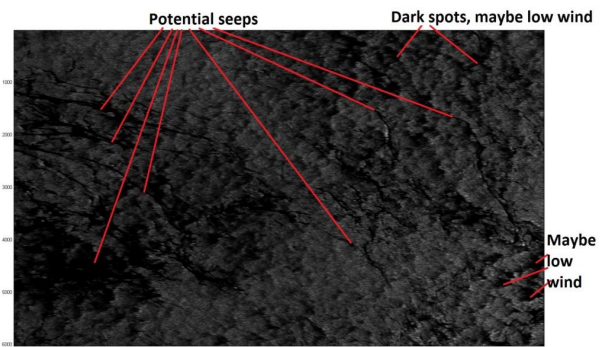
(a) Gray scale image from the vv-channel of the OPV scene



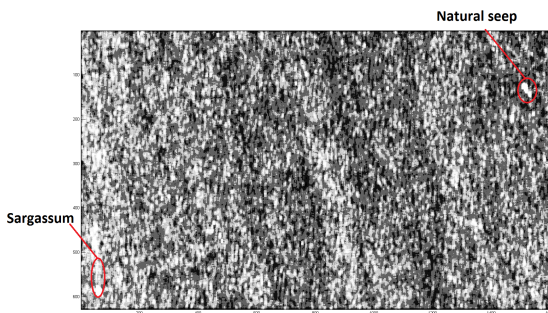
(b) Gray scale image from the vv-channel of image #1



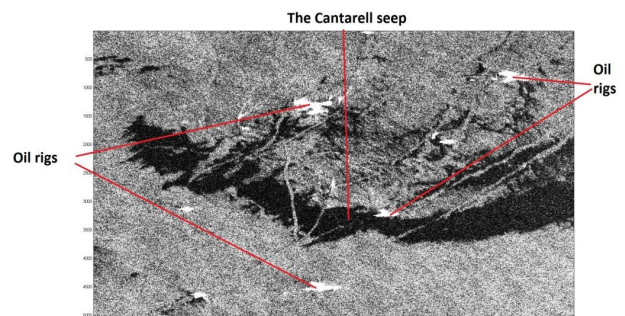
(c) Gray scale image from the vv-channel of image #2



(d) Gray scale image from the vv-channel of image #3



(e) Gray scale image from the vv-channel of image #4



(f) Gray scale image from the vv-channel of image #5

Figure 5.4: The SAR-subscenes that is processed in this thesis. Indication of what the images contains.

Chapter 6

Methodology

The methods used in this thesis are eigenvector-eigenvalue decomposition, polarimetric feature extraction, derivation of scatterplots and histograms, segmentations of dark spots and classification with a supervised maximum likelihood classifier. How these methods are performed and applied to the images is described in this chapter.

6.1 Eigenvector-eigenvalue decomposition

The coherency matrix and the covariance matrix defined in section 2.4 are used in this thesis for target decomposition and calculation of polarimetric features in Matlab. First we will look at the $H/A/\alpha$ -decomposition, which is an eigenvector-eigenvalue based decomposition [66] from the coherency matrix. The coherency matrix can be written as:

$$[\mathbf{T}] = [\mathbf{U}][\mathbf{\Sigma}][\mathbf{U}] \quad (6.1)$$

where $[\mathbf{\Sigma}]$ is a $d \times d$ matrix, $d = 2$ in this case because the crosspol-channels are excluded, containing the eigenvalues of the coherency matrix:

$$[\mathbf{\Sigma}] = \begin{bmatrix} \lambda_1 & 0 \\ 0 & \lambda_2 \end{bmatrix} \quad (6.2)$$

where $\lambda_1 > \lambda_2$, and $[\mathbf{U}]$ is a 2×2 matrix containing the eigenvectors:

$$[\mathbf{U}] = [u_1 \ u_2] \quad (6.3)$$

The eigenvectors are given as:

$$u_i = [\cos\alpha_i \ \sin\alpha_i \cos\beta_i e^{j\delta_i}] \quad (6.4)$$

for $i = 1, 2$. If we put equations 6.2-6.4 into equation 6.1 the expression for the coherency matrix [66] becomes:

$$[\mathbf{T}] = \sum_{i=1}^2 \lambda_i u_i u_i^{*T} \quad (6.5)$$

All the features defined below can be found in Skrunes et al. [21].

6.1.1 Entropy H

The entropy H is a measure of how random the scattering is [66] and is defined for $d = 2$ as:

$$\mathbf{H} = - \sum_{i=1}^2 p_i \log_2(p_i) \quad p_i = \frac{\lambda_i}{\lambda_1 + \lambda_2} \quad (6.6)$$

where p_i is the probability of the eigenvalues. The entropy takes values between 0 and 1. If $H = 0$ there is no randomness of the scattering, $\lambda_1 = SPAN$ and $\lambda_2 = 0$ ($\lambda_1 > \lambda_2$), where $SPAN = \sum_{i=1}^2 \lambda_i$ is the total scattered power, and we are looking at a target. When $H = 1$ there is a mixture of different scattering mechanisms, but also indication of noise and $\lambda_1 = SPAN/2$ and $\lambda_2 = SPAN/2$. $0 < H < 1$ depends on which target is the most dominating. Smooth ocean surfaces have small entropy due to the one dominating scattering mechanism. Sea surface areas covered with oil usually have greater values [20], however, Minchew et al. [1] state that the entropy only is increased when the signal is close to the noise floor.

6.1.2 Mean scattering angle $\bar{\alpha}$

The mean scattering angle α is defined as:

$$\bar{\alpha} = \sum_{i=1}^2 p_i \alpha_i \quad (6.7)$$

where $\bar{\alpha}$ is the angle from the eigenvector in 6.4. $\bar{\alpha}$ indicates which scattering mechanism is the dominating one. For small values of $\bar{\alpha}$ there is a surface scattering, for large values there is double bounce and medium ($\bar{\alpha} = 45$) indicates a volume scattering [67].

6.1.3 Anisotropy A

Anisotropy measures the relative importance of the eigenvalues and is given as:

$$\mathbf{A} = \frac{\lambda_1 - \lambda_2}{\lambda_1 + \lambda_2} \quad (6.8)$$

Slick free areas at the ocean surface usually have anisotropy values close to 1 ($\lambda_1 \gg \lambda_2$), which indicates that there is only one scattering process dominating [20]. Areas covered with oil have less anisotropy values, which means more contribution from the second eigenvalue and indicates there are several scattering mechanisms in this area.

6.2 Polarimetric features from the covariance matrix

The first set of features were derived from the decomposition of the coherence matrix. The next set of features is derived from the components of the covariance matrix.

6.2.1 Mean radar backscatter μ

Mean radar backscatter measures the brightness in the image [20] and is derived from the covariance matrix as:

$$\mu = |\det([\mathbf{C}])|^{1/d} \quad (6.9)$$

Since μ values are brightness measures, areas covered with oil should have low values due to the dampening of capillary waves, while oil-free areas should have higher values due to rougher surface.

6.2.2 Co-polarization ratio γ_{co}

The co-polarization ratio is also derived from the covariance matrix by using the first and fourth element of the matrix:

$$\gamma_{co} = \frac{\langle |S_{hh}|^2 \rangle}{\langle |S_{vv}|^2 \rangle} \quad (6.10)$$

It's the magnitude of the hh-channel divided by the magnitude of the vv-channel. γ_{co} is independent of the roughness of the surface and only depends on the dielectric constant, the incidence angle and the root mean square error of the target [20].

6.2.3 Standard deviation (std) of the co-polarized phase difference (CPD)

The std. of the CPD is given as:

$$\sigma_{\phi_{co}} = \sqrt{(\langle (\phi_{hh} - \phi_{vv})^2 \rangle - (\langle \phi_{hh} - \phi_{vv} \rangle)^2)} \quad (6.11)$$

where ϕ_{hh} and ϕ_{vv} are the phases of the HH- and VV-channel. The CPD's distribution is determined by two parameters. First of all the correlation between the HH- and VV-channel of the scattering matrix and secondly the value of ϕ_{co} which corresponds to the maximum value of the distribution [20]. Oil free areas have high correlation between the HH- and VV-channel and therefore a narrow CPD-pdf and a low $\sigma_{\phi_{co}}$ value. Surfaces covered with oil however, have low correlation between the co-polarized channels and a more wider CPD-pdf and a high $\sigma_{\phi_{co}}$ value [68], [69] and [70].

6.2.4 Correlation magnitude ρ_{co}

The correlation magnitude is given as:

$$\rho_{co} = \left| \frac{\langle S_{hh} S_{vv}^* \rangle}{\sqrt{\langle |S_{hh}|^2 \rangle \langle |S_{vv}|^2 \rangle}} \right| \quad (6.12)$$

and gives an indication of how related the signals of the co-polarized channels are. If ρ_{co} has a value of 1 it means the backscattered signal of the co-polarized channels are linearly related. If $\rho_{co} < 1$, the channels are not so related and usually contain noise [67].

6.2.5 Real part of the co-polarization correlation r_{co}

This correlation is defined as:

$$r_{co} = |\Re(\langle S_{hh} S_{vv}^* \rangle)| \quad (6.13)$$

where the real part is denoted by \Re . r_{co} usually have higher sea values than oil values because of the decreased correlation with more than one scattering mechanism [20].

6.3 Statistical methods and preprocessing

Scatter plots of the polarimetric features that gave best separability between oil and water are made. Pixel values from small regions, a box of 2500 pixels, are taken from the features at interesting positions indicated in figure 6.1 in all the images. For image #4 smaller boxes are used, 50 – 100 pixels. To make these plots, the points are plotted for one feature on the x-axis and for another on the y-axis. The same points are used to create histograms.

6.4 Classification

The classification done based on the polarimetric features in this thesis will be performed in two steps. First of all a segmentation of the potential slicks in the images will be done. Secondly a supervised classification will be used with the OPV-scene as a training set. The test set is the oil-segmented areas of the GoM-scenes to make an attempt to assign the dark patches in the scenes as either oil-slicks or look-alikes.

6.4.1 Segmentation of the dark spots

The first step in the classification is to segment out the dark regions that are potential oil-slicks. This is done for the Gulf-scenes (except image #4 and #5) with the conformity coefficient and by a threshold in the features for the OPV-scene and image #5. For the OPV-scene, a pixel is set to water if $\mu > -6.2$ dB and $r_{co} > -5.3$ dB. In image #5 it is water if $r_{co} > -5$ dB.

The conformity coefficient has been used in previous studies for estimation of soil moisture. In 2011, Zhang et al. [19] developed a method to use the conformity coefficient to discriminate oil-slicks from water. The coefficient is defined as:

$$\mu_{cc} = \frac{2(\Re(S_{hh}S_{vv}^*) - |S_{hv}|^2)}{|S_{hh}|^2 + 2|S_{hv}|^2 + |S_{vv}|^2} \quad (6.14)$$

In oil free areas the co-polarized channels are strongly correlated while the signal in the cross-polarized channels is more close to zero. This indicates that $(\Re(S_{hh}S_{vv}^*)) > |S_{hv}|^2$ which should give a positive μ_{cc} value. For slick-covered areas the correlation between the co-polarized channels is much lower due to a more random scattering, therefore $|S_{hv}|^2 > (\Re(S_{hh}S_{vv}^*))$ and the value of μ_{cc} should be negative. This is the method Zhang et al. [19] used to discriminate oil-slicks from water. For the dataset in this study, the coefficient manage to segment out the dark patches from the Gulf, but failed with the OPV-scene because all the pixel values were above zero. This may have to do with different weather conditions, incidence angle and the image contains boats. The segmented areas are given in figure 6.2.

6.4.2 Supervised maximum likelihood classification

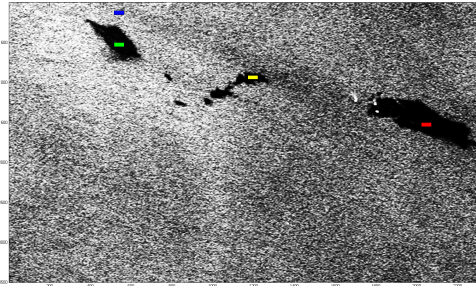
In this thesis a trained maximum likelihood classifier is used. As training data, all the pixels from the boxes in figure 6.1 (a) are used. Baye's Decision rule is defined as:

$$\text{Decide } \omega_i \text{ if } p(\mathbf{x}|\omega_i)P(\omega_i) > p(\mathbf{x}|\omega_j)P(\omega_j) \quad (6.15)$$

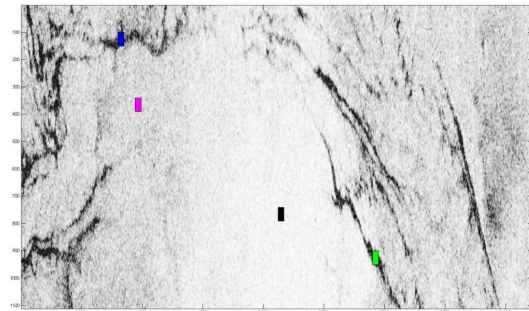
where $P(\omega_j)$ are the prior probabilities and $p(\mathbf{x}|\omega_j)$ is the likelihood of w_j with respect to the feature vector \mathbf{x} . The priors are assumed to be equal so the classes are equally probable and the decision is based entirely on the likelihood. The approach from here is to generate a set of discriminant functions, $g_c(\mathbf{x})$, $c = 0, 1, 2$, where c are the classes 0=water, 1=emulsion and crude-oil, and 2=plant-oil. The classifier is then supposed to assign the feature vector \mathbf{x} to class i if:

$$g_i(\mathbf{x}) > g_j(\mathbf{x}) \quad j \neq i \quad (6.16)$$

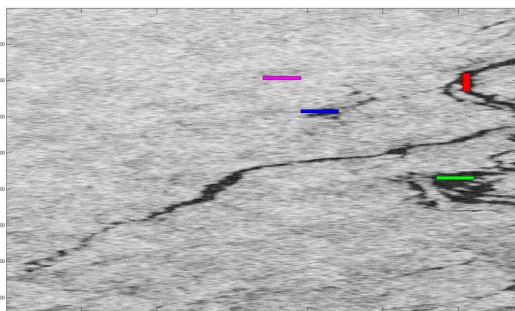
The data are assumed to be normal distributed based on observations from the histograms which will be presented in section 7.3. The multivariate normal density is defined as:



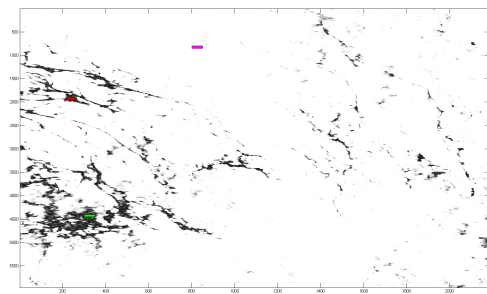
(a) Gray scale image from the anisotropy of the OPV scene



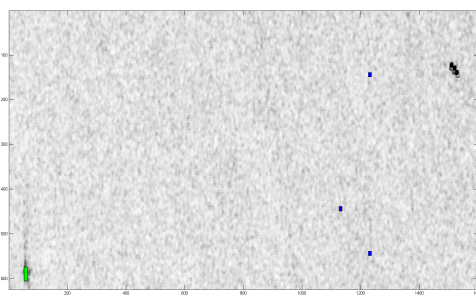
(b) Gray scale image from the anisotropy of image #1



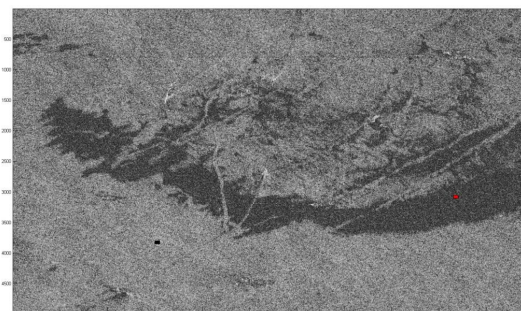
(c) Gray scale image from the anisotropy of image #2



(d) Gray scale image from the anisotropy of image #3

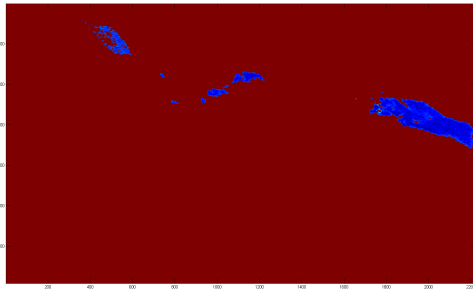


(e) Gray scale image from the anisotropy of image #4

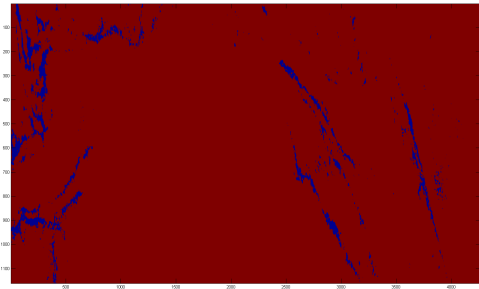


(f) Gray scale image from the anisotropy of image #5

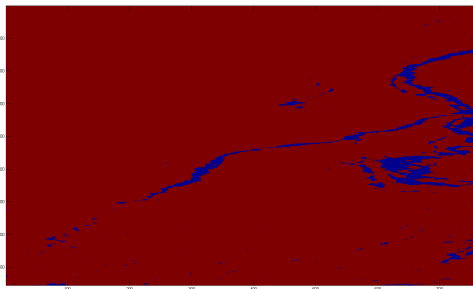
Figure 6.1: SAR-subscenes with indication where the pixel values for the scatter plots are taken, each box consist of 2500 pixels, except for iamge #4 which varies from 50-150



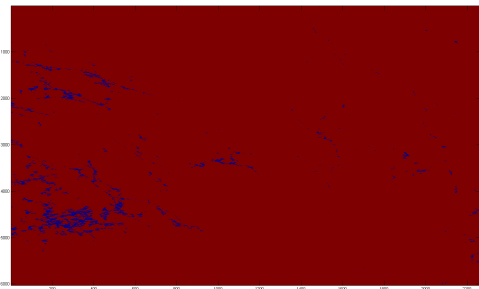
(a) The OPV-segmented by thresholding



(b) #1 image segmented by the conformity coefficient



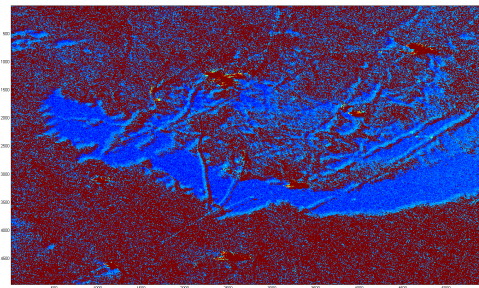
(c) #2 image segmented by the conformity coefficient



(d) #3 image segmented by the conformity coefficient



(e) #4 image segmented by the conformity coefficient



(f) #5 image segmented by thresholding

Figure 6.2: Segmentation of slick regions

$$p(x) = \frac{1}{(2\pi)^{d/2} |\Sigma|^{1/2}} \exp\left[-\frac{1}{2}(\mathbf{x} - \mu) \Sigma^{-1} (\mathbf{x} - \mu)\right] \quad (6.17)$$

where d is the dimension, μ the mean vector with d -components, Σ is the covariance matrix of the used features (not the same as defined in section 2.4) of size $d \times d$, $|\Sigma|$ its determinant, Σ^{-1} the invers and \mathbf{x} is the feature vector. The discriminant function for the normal density varies depending on the covariance matrix, whether it is equal for all classes, if it is diagonal (the features are statistically independent and have the same variance) or the covariance matrices for every class are arbitrary. For the OPV- and GoM-scenes, the covariance matrices are arbitrary or different and the discriminant function for the classifier is defined as:

$$g_c(x) = -\frac{1}{2}(\mathbf{x} - \mu_c)^t \Sigma_c^{-1} (\mathbf{x} - \mu_c) - \frac{d}{2} \ln 2\pi - \frac{1}{2} \ln |\Sigma_c| - \ln P(\omega_c) \quad (6.18)$$

Σ_c and μ_c are derived from the OPV-scene for the different classes, then the discriminant functions derive the probability that a pixel is in one of the different classes and the classifier assign it to the most probable. This is done for all not-water pixels in the images [71].

6.5 Signal to noise analysis

Due to all the low backscattering areas in the images, a signal to noise system analysis has been performed. The radar backscatter for the dark regions is compared to the noise floor to see if it lies higher. If not, there is a risk that the signal is corrupted by noise. The same areas used for scattering plots and histograms marked in figure 6.1 are used here. The mean and standard deviation of the different regions are derived. Then they are plotted with the mean as sentrum with a bar of one deviation down and one deviation up. The noise analysis is not performed for image #5 because of trouble in the Matlab-codes.

Chapter 7

Results and discussion

The aim with this thesis was to investigate seep with multi-polarized SAR-images and compare values from seeps with values from biogenic and mineral slicks. The six images presented in chapter 5 have been processed and investigated with polarimetric features and statistic from these. The images with potential seeps have also been classified. All the results from the methods described in chapter 6 are presented here. Section 7.1 presents all the polarimetric features extracted from the scenes. Section 7.2 and 7.3 includes the scatterplots and histograms from some of the features. In section 7.4 the signal-to-noise is presented and section 7.5 shows the classification. Section 7.6 is a discussion of the scenes.

7.1 Presentation of the values from the polarimetric features

All the polarimetric features from Skrunes et al. [20] are presented in this section. A visual inspection has been made and also some discussion of what the results tell. The μ, γ_{co} and r_{co} are log-transformed so they give better contrast and therefore the values are given as dB. Table 7.1 gives an overview of all the different oil values in all the polarimetric features.

Entropy H

The entropy can be seen in figure 7.1 (a) - 7.6 (a). The crude-oil from the OPV-scene have values around 0.6 to 0.9, while the GoM-scenes, except image #4, have values from 0.7 to 1. The water lies for the OPV-scene around 0.1 to 0.3, in image #1 from 0.2 to 0.7 (light and dark water), in #2 from 0.4 to 0.8, in image #3 from 0.1 to 0.2, in image #4 from 0.2 to 0.7 and in #5 from 0.6 up to 0.9. In all the images, the sea has a low entropy, which can indicate a single scattering mechanism. The crude and emulsion oil in figure 7.1 (a) and the dark slicks in figure 7.2 (a)-7.6 (a) have higher entropy values, so a more complex scattering is present but also high entropy values means the signal could be corrupted by noise. The plant-oil in figure 7.1 (a) has values between the crude-oil and the sea. The entropy gives a very good contrast between oil and water in all the figures.

Mean scattering angle $\bar{\alpha}$

$\bar{\alpha}$ is given in figure 7.1 (b) - 7.6 (b). In the OPV-scene and image #3 the sea has values around 10° to 20° , in image #1 and #2 from 20° to 30° , in image #5 from 25° to 35° and in image #5 from 60° to 70° . The emulsion and crude-oil for the OPV-scene lie around 40° to 45° , for image #1, #2, #3 and #5 from 45° to 50° and in image #4 from 42° to 45° . For the mean scattering angle results, the sea surface have low values for the OPV-scene and image #1 - #4 which means there is a surface scattering. The slick covered areas in the OPV-scene and image #1 - #4 have greater values, most of them around 45° , which is at the limit of a Bragg-scattering mechanism according to the H/α plane [20]. But this is when the \mathbf{T} -matrix is three dimensional, in this thesis it is only two dimensional which can change the limit. A really interesting thing here is the plant oil in the OPV image, figure 7.1 (b), which is almost gone. The plant-oil can be spotted to a certain limit so the

$\bar{\alpha}$ looks promising to discriminate between oil-slicks and look-alikes.

Anisotropy A

The anisotropy feature can be seen in figure 7.1 (c) - 7.6 (c). The emulsion and crude-oil in the OPV-scene take values from 0.2 to 0.8, in image #1 the oil lies from close to 0 up to 0.7, in image #2 from around 0 to 0.6, in image #3 from close to 0 up to 0.5 and in image #5 from 0 to 0.6. The water values are for the OPV-scene from 0.9 to 1, in image #1 from 0.6 to 0.9, in image #2 from 0.5 to 0.8, in image #3 from 0.9 to 1 and in image #5 from 0.2 up to 0.8. For the derived anisotropy images, figure 7.1 (c) - 7.6 (c), the sea has high values which means $\lambda_1 \gg \lambda_2$ and, as mentioned about the entropy, there is only one scattering mechanism. For the slick covered areas the values are lower. This indicates more contribution from λ_2 . The anisotropy also gives a good oil to water contrast.

Mean radar backscatter μ

The mean radar backscatter is given in figure 7.1 (d) - 7.6 (d). The oil lies for the OPV-scene from -6 to -7, in image #1 from -6.7 dB to -7.7 dB, in #2 from -6.5 dB to -7.5 dB, in image #3 from -3 dB to -3.6 dB and in image #5 from -3.7 dB down to -5 dB. The water values are for the OPV-scene from -4.4 dB to -5.4 dB, in image #1 from -5.4 dB to -6.9 dB, in image #2 from -6.2 dB to -6.6 dB, in image #3 from -1.9 dB to -2.2 dB and in image #5 from -3.5 dB to -4.5 dB. For image #4 the seep actually have higher values than sea. The sea has values around -6 dB while the seep lies around -3.5 dB and the sargassum have values up to -1 dB. So, it looks like the sea has a smoother surface than the seep and the sargassum which is really unusual. This makes it more questionable if the information about this scene is correct. In all the other images the oil covered areas take the lowest values indicating a smoother surface than the surroundings. The contrast between oil and water is good for all the figures. The oilrigs and boats in image #5 in figure 7.6 (d) can be seen as strong point targets. μ gives a good slick to sea contrast for the Radarsat-2 images, but a moderate contrast for the TerraSAR-X-scene, image #5.

Co-polarization ratio γ_{co}

γ_{co} can be found in figure 7.1 (e) - 7.6 (e). In this feature the oil have values around -0.3 dB for all the images. The water in the OPV-scene have values around -0.5 dB, in image #1 and #2 around -1.2 dB to -0.5 dB, in image #3 around -0.5 dB up to -0.3 dB, in image #4 from -1.5 dB to -0.7 dB and in image #5 from -0.5 dB up to -0.3 dB. In other words, the oil slicks have higher values than the sea around. This may have to do with change in dielectric constant between oil and water [20]. The contrast in the figures is quite moderate and even low in figure 7.4 (e) where the slicks almost can't be seen. This may have to do with the incidence angle of image #3. As mentioned in section 6.2.2, γ_{co} is dependent of the incidence angle and as seen from Table 5.1, image #3 have lower incidence angle than all the other images.

Standard deviation of the CPD $\sigma_{\phi_{co}}$

The derived $\sigma_{\phi_{co}}$ can be found in figure 7.1 (f) - 7.6 (f). In the OPV-scene, image #1, #2, #3 the oil have values around 1.2 to 1.5, in image #4 the oil is from 1.7 to 2.2 and in image #5 around 2. The water for all the images lies from 0.5 to 1.2. The results show that the sea has lower values than the slick covered areas. So, in all the images, the co-polarized channels are more correlated in the sea areas than the oil areas. The contrast between oil and water is moderate.

Image	OPV	#1	#2	#3	#4	#5
H	c: 0.6-0.9, e: 0.6-0.9, p: 0.2-0.6	ps: 0.7-1	ps: 0.7-1	ps: 0.7-1	s: 0.4-0.75, sa: 0.4-0.7	s: 0.7-1
$\bar{\alpha}$	c: $40^\circ - 45^\circ$, e: $40^\circ - 45^\circ$, p: $20^\circ - 25^\circ$	ps: $45^\circ - 50^\circ$	ps: $45^\circ - 50^\circ$	ps: $45^\circ - 50^\circ$	ps: $42^\circ - 45^\circ$, sa: $42^\circ - 45^\circ$	s: $45^\circ - 50^\circ$
A	c: 0.2-0.8, e: 0.2-0.8, p: 0.7-0.9	ps: 0-0.7	ps: 0-0.6	ps: 0-0.5	s: 0.55-0.85, sa: 0.6-0.8	s: 0-0.6
μ	c: -6dB to -7dB, e: -6dB to -7dB, p: -5.5dB to -6 dB	ps: -6.7dB to -7.7dB	ps: -6.5dB to -7.5dB	ps: -3dB to -3.6dB	s: -5.6dB to -6.5dB, sa: -5.6dB to -6.5dB	s: -4dB to -5dB
γ_{co}	c: -0.8dB to 0.5dB, e: -1dB to 0.5 dB, p: -1dB to 0.1 dB	ps: -1dB to 0.5 dB	ps: -1dB to 0.5 dB	ps: -1dB to 0.5 dB	s: -1dB to -0.5 dB, sa: -1dB to -0.5 dB	s: -1dB to 0.5 dB
σ_{co}	c: 1.2-1.5, e: 1.2-1.5, p: 1-1.2	ps: 1.2-1.5	ps: 1.2-1.5	ps: 1.2-1.5	s: 1.7-2.2, sa: 1.7-2.2	s: 2
ρ_{co}	c: 0.2-0.8, e: 0.2-0.8, p: 0.7-0.9	ps: 0-0.6	ps: 0-0.6	ps: 0-0.8	s: 0.6-0.8, sa: 0.6-0.8	s: 0-0.5
r_{co}	c: -6dB to -8.2dB, e: -5.5dB to -8dB, p: -6dB to -4dB	ps: -14dB to -8dB	ps: -14dB to -8dB	ps: -14dB to -8dB	s: -6.5db to -5.5dB, sa -6.5db to -5.5dB	s: -10dB to -5dB

Table 7.1: Overview of all the oil-slick values. c=crude-oil, e=emulsion, p=plant-oil, ps=potential seep, s=seep, sa=sargassum

Correlation magnitude ρ_{co}

ρ_{co} is given in figure 7.1 (g) - 7.6 (g). The emulsion and crude-oil lie here around 0.6 while the plant-oil around 0.7 and for the rest of the images the oil lies around 0.1 to 0.4. So, the sea has greater values than the slick covered areas. The reason for this is probably the present of more than one scattering mechanism in the slick areas. Kasilingam et al. [72] meant that the decrease in ρ_{co} is not from roughness but change in dielectric constant. ρ_{co} gives a good contrast between oil and water for all the images.

Real part of the co-polarization correlation r_{co}

As seen from the plots in figure 7.1 (h) - 7.6 (h), the oil areas from the GoM-scenes lies from -8 dB to -14 dB on the r_{co} while the crude- and emulsion-oil lies between -6 dB and -8 dB. The water for the OPV-scene lies from -3 dB to -4.5 dB, for image #1 it lies from -4 dB to -8 dB, for image #2 from -6 dB to -8 dB, for image #3 between -2 dB and -4 dB and for image #5 from -5 dB to -13 dB. In figure 7.1 (h) - 7.6 (h) we can see that the correlation is less for the slick-covered areas than the ocean surface. This could be due to the present of more than one scattering mechanism in the slick-covered areas [20]. r_{co} gives a good contrast between oil and water for all the images.

7.2 Results of the scatterplots

The polarimetric features used in the scatterplots are chosen based on observation from last section. H, μ, A and r_{co} are chosen because of the good contrast between oil and water. γ_{co} however have been chosen because it is also interesting to investigate the dielectric properties of the different slicks.

7.2.1 Entropy vs. mean radar backscatter

In figure 7.7 the scatter plots of entropy vs. the mean radar backscatter are given for all six scenes. For the OPV-scene in figure 7.7 (a) we can see that the water and plant-oil points form two separate clusters in both the H - and μ -axis. The emulsion and crude-oil are mostly overlapping and create one separate cluster, although the crude-oil has mostly the highest values on the H -axis and the emulsion has higher variation. For image #1 in figure 7.7 (b) the light water area and the two oil patches make their own clusters. The dark water area makes a third cluster between and slightly overlapped by some of the oil points. For image #2 and #3 in figure 7.7 (c) and (d) the water and the oil patches clearly stand out as two different clusters in both plots. For image #4 in figure 7.7 (e), the pixels are spread randomly around and the sargassum, the water and the seep are overlapping with each other. The scatterplot for image #5 in figure 7.7 (f) have two slightly overlapping clusters for the water and the Cantarell seep. The water values are similar between the OPV-scene and image #3 and between #1 and #2 in the H -axis. For the μ -axis, the values are similar for the OPV-scene, image #1 and #2, but not for image #3 or #5. In the scatterplot for image #4 all the values are spread from -5.6 to -6.5 on the μ -axis and from 0.35 up to 0.75 on the H -axis. As we can see from the values mentioned, the slick-covered areas lie a little bit higher on the H -axis for the Gulf of Mexico scenes than the OPV-scene. On the μ -axis the oil have similar values for the OPV-scene, image #1 and #2, but for the #3 and #5 the oil have higher values.

7.2.2 Anisotropy vs. mean radar backscatter

The scatter plots of anisotropy vs. mean radar backscatter can be seen in figure 7.8. The plant-oil and the water in the OPV-scene make two clusters in figure 7.8(a) in both the A and μ -axis, the plant oil a little bit overlapped by the emulsion-oil. Last cluster is formed by the emulsion and crude-oil. For image #1 in figure 7.8 (b) the water areas make their own clusters and the oil areas make one cluster. In figure 7.8 (c) and (d), the water and oil also stand out as two different clusters. For image #5 in figure 7.8 (f) the water and seep make two clusters, but they are a little bit overlapped. If the results in figure 7.8 are compared with the results in 7.7, it can be seen that the clusters are almost the same, the only difference is that the values at the A -axis for water and oil is opposite from the H -axis. As seen from figure 7.8, the slick-covered areas from the Gulf have lower values than the oil in the OPV-scene on the A -axis. Also the water values from the GoM-scenes are lower than the water in the OPV-scene.

7.2.3 Real part of the co-polarization correlation vs. mean radar backscatter

The scatterplots can be seen in figure 7.9. For the OPV-scene in figure 7.9(a) the same clusters mentioned in section 7.2.1 and 7.2.2 occur. The dark water in image #1 is a little bit overlapping with the oil. In image #2 and #3 the oil and water make their own clusters. For the TerraSAR-X image, the clusters are much less overlapped in the r_{co} -axis compared to the feature axis in section 7.2.1 and 7.2.2.

7.2.4 Real part of the co-polarization correlation vs. correlation magnitude

The plots are given in figure 7.10. Here we also have the clusters mentioned in H vs μ and A vs μ , but there are more overlap in the ρ_{co} -axis than in the other plots except for image #3. The crude- and emulsion-oil for the OPV scene takes values from 0.2 to 0.8 on the ρ_{co} -axis, the oil areas in image #1 are between 0 and 0.6, for image #2 they are between 0 and 0.5, in image #3 they are between 0 and 0.4 and for image #5 they are from 0 to 0.6. The water in the OPV-scene are from 0.8 to 1, in image #1 and #2 they lie from 0.3 to 1, for image #3 they lie from 0.9 to 1 and in image #5 from 0 to 0.8.

7.3 Results of Histograms

The features used to create the histograms in this section are chosen based on the same reasons mentioned in section 7.2. When the histograms were created, the amount of one pixel value was divided by the total amount of pixel values. So the values on the y-axis in the histograms represent the probabilities of the pixel values on the x-axis.

7.3.1 Histograms of H

In figure 7.11 histograms of H from all the images can be seen. From the OPV-scene in figure 7.11 (a) the water make its own pdf separated from the oil, same as for the plant-oil in the middle while emulsion and crude-oil overlap each other. In the rest, the slick-covered areas make one pdf and water another. So, H looks like a good feature to distinguish between oil and water. One thing to notice is that the oil from the OPV-scene has more variation than the slick-covered areas from the Gulf. All the histograms reminds of Gaussian distributions, but they are not ideal. The skewness observed in figure 7.11 (b)-(d) can be explained by the fact that there are some water pixels in the selected areas. This also explains the points that connect the clusters in figure 7.7-7.10 (b)-(d). The histograms for image #4 are really badly overlapped, most likely because there are very few pixel points from the seep and sargassum to work with.

7.3.2 Histograms of μ

The μ histograms are given in figure 7.12 and the pdfs are separated as in the H -histograms. Some differences though can be noticed. In figure 7.12 (a) the crude- and the emulsion-oil are more overlapping and the distribution from the different areas are more equal. Also for the μ histograms it looks like the slick-covered areas from the Gulf have more the same distribution as the oil in the OPV-scene, but not the same values. The histograms are narrower for the μ feature vector than for the H .

7.3.3 Histograms of r_{co}

These histograms are given in figure 7.13. The same pdfs appear in these histograms too and the biggest thing to notice is that the slick-covered areas from the Gulf have larger variance than the water for image #1-#3.

7.3.4 Histograms of ρ_{co}

Histograms from the ρ_{co} feature vector are given in figure 7.14. All the mentioned pdfs stand out in the histograms of all the images except #4. One thing to notice from these histograms is that the oil from the Gulf (#1, #2, #3, #5) looks more Rayleigh distributed than Gaussian due to the skew towards the right side.

7.3.5 Histograms of γ_{co}

These histograms can be found in figure 7.15. To the difference from the other histograms mentioned, in γ_{co} the pdfs are more overlapped with each other. In the OPV-scene, figure 7.15 (a), the plant oil is overlapping with the emulsion and crude oil. Also a big part of the water is overlapping with the oil. For image #1 and #2 in figure 7.15 (b) and (c) the oil and water make two clusters, but there is some overlap here too. In image #3 and #5 the oil is completely overlapped by the water, which makes sense since the slicks almost can't be seen in figure 7.4 (e) and figure 7.6 (e). The co-polarization ratio seems to be a bad feature for distinguishing between oil and water. However, the co-polarization ratio seems to be the only feature where the oil have almost the same values (-0.3 dB) in all the scenes, except image #4.

7.4 Results of signal-to-noise analysis

The signal-to-noise analysis can be found in figure 7.16. The plots reveal that all the oil bars are crossing the noise floor. In image #1 the mean of the oil patches are actually beneath the noise floor and the dark water

patches are slightly crossing the noise floor. The mean values of the oil patches from image #2 are also beneath the noise floor and the water is crossing it, but the mean values are above. For image #3 the oil patches only touching the noise floor, the mean values are above and the water values are far above. Image #4 have all the mean values above the noise floor, but all the bars are crossing the noise floor. Another thing to observe is that in every case, the VV-channel contains less noise than the vv-channel. According to Minchew et al. [1], all data that has backscatter less than 6 dB above the noise floor is noise corrupted. So, all the Radarsat-2 images contains a certain amount of noise, especially image #1 and #2.

7.5 Classification results

Observed from the previous results including scatter plots, histograms and the features, decision was made to classify based on the mean radar backscatter and entropy separately. The main reason is the small overlap in the histograms and the good slick to sea contrast from the feature images. Image #4 is excluded from the classification because there is not enough values in the seep or the sargassum, and also the suspicion of not right information about the scene. The classified images can be seen in figure 7.17 and 7.18. In the classified images based on the mean radar backscatter feature vector in figure 7.17 almost every part of the dark patches in the scenes is classified as oil. Only in image #1 there are small areas in the slicks that are classified as plant oil or look-alike. For the classification based on the entropy in figure 7.18 most of the slicks are classified as oil here too. But in this case more areas in image #1 and also in image #2 and #3 are classified as plant-oil. Image #5 is almost only classified as oil or water. A lot of water pixel in these two classifications has been classified as oil instead. But as seen from the histograms in figure 7.11 (f) and 7.12 (f) the oil and water are overlapping, which will make some of the water pixels mistaken as oil pixels and opposite.

The result of some parts classified as plant oil is not surprising because oil slicks have thinner areas, usually around the edges between oil and sea. So the areas classified as plant oil can be places where the slicks are thinner than the rest of the slick. The surprising thing by these areas is where they are located. As seen from figure 7.17 (a) and 7.18 (a)-(c) the areas are not only around the edges, but also spread inside the slicks. So it looks like there must be variations inside the slicks.

7.6 Discussion of the scenes

From the results given in section 7.1 - 7.4, there are different things that have to be pointed out. First of all the GoM-scenes have to be considered. From the results in section 7.1-7.3 the dark patches show similar, but not the same, results as the crude and emulsion-oil from the OPV-scene. Also the classification stated that the slicks are most similar to emulsion and crude-oil. Another thing to be pointed out is the location of the slicks with no sign of vessels or rigs. So, either the ships are gone or the source of the slicks in image #1, #2 and #3 must come from beneath the surface, either a seep or a leaking pipeline.

Even though there are similarities, in most of the cases there are differences between the slick values in the polarimetric features. In some of the features, like H , r_{co} , ρ_{co} and A , the Gulf-scenes seem to have similar values to each other but different from the OPV-scene. The GoM-scenes have higher entropy values and lower anisotropy values which can be explained by the signal-to-noise observation from section 7.4. Compared to Skrunes et al. [21], the slicks from the GoM-scenes are closer to the noise floor than the OPV-scene which can cause greater entropy values and lower anisotropy values. Differences in the r_{co} indicate that the scattering processes in the different scenes are not totally the same. ρ_{co} also show such differences which can indicate some variety in the scattering mechanism. This can be explained by different sea-states and incidence angles between the scenes since the water values are different too.

Another thing to point out is that for the γ_{co} feature, the oil have approximately the same values for all

the scenes, but the water have different values. So, the slicks from the GoM-scenes may have similar dielectric properties as the crude-oil, emulsion and plant-oil from the North Sea. For the μ feature vector, the values of the slicks and sea seem to vary a lot more between the scenes. Since this is a brightness measure, μ is affected by parameters like wind speed which varies between the scenes, see table 1 in Chapter 5.

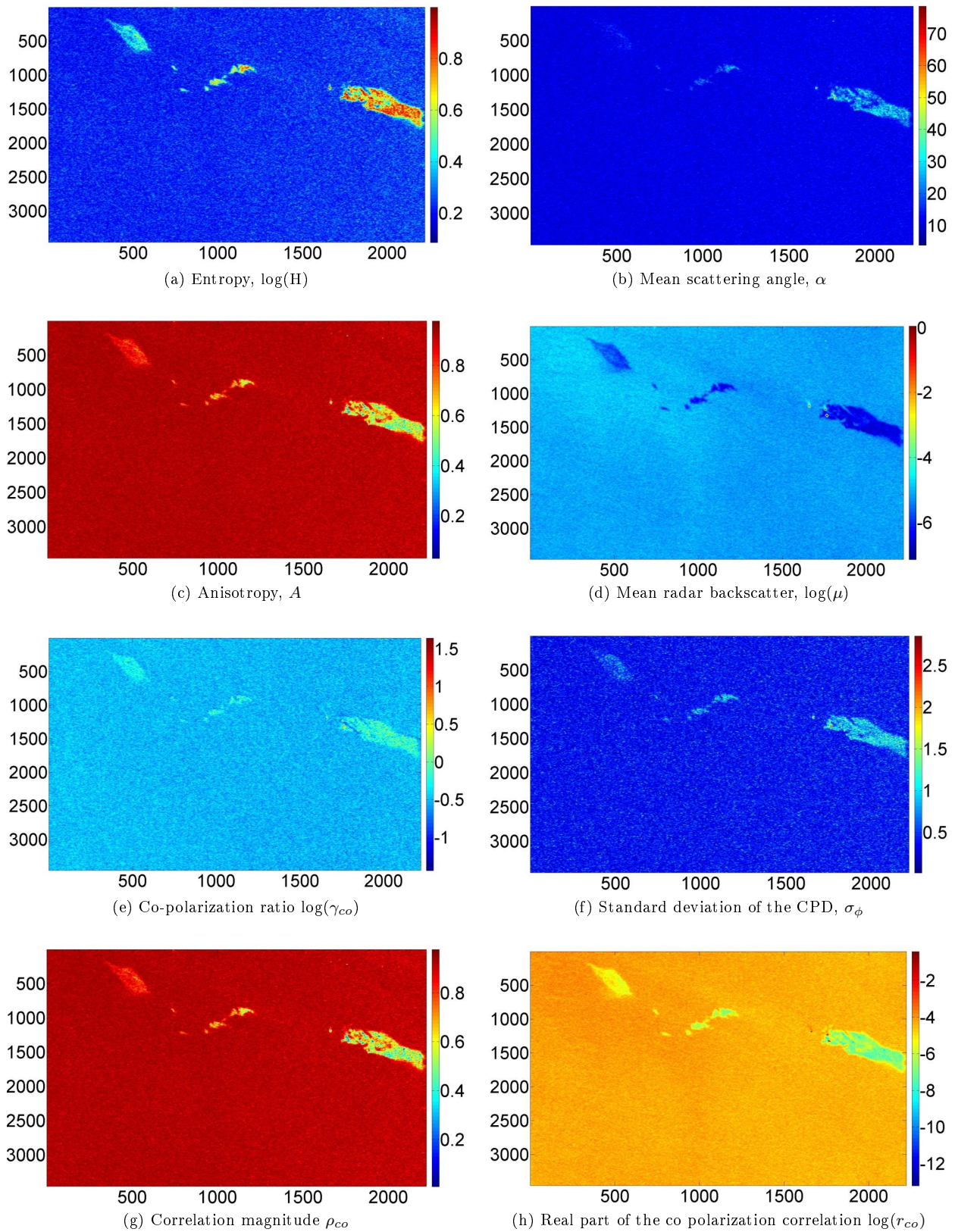


Figure 7.1: Multi-polarization features calculated from the OPV-scene

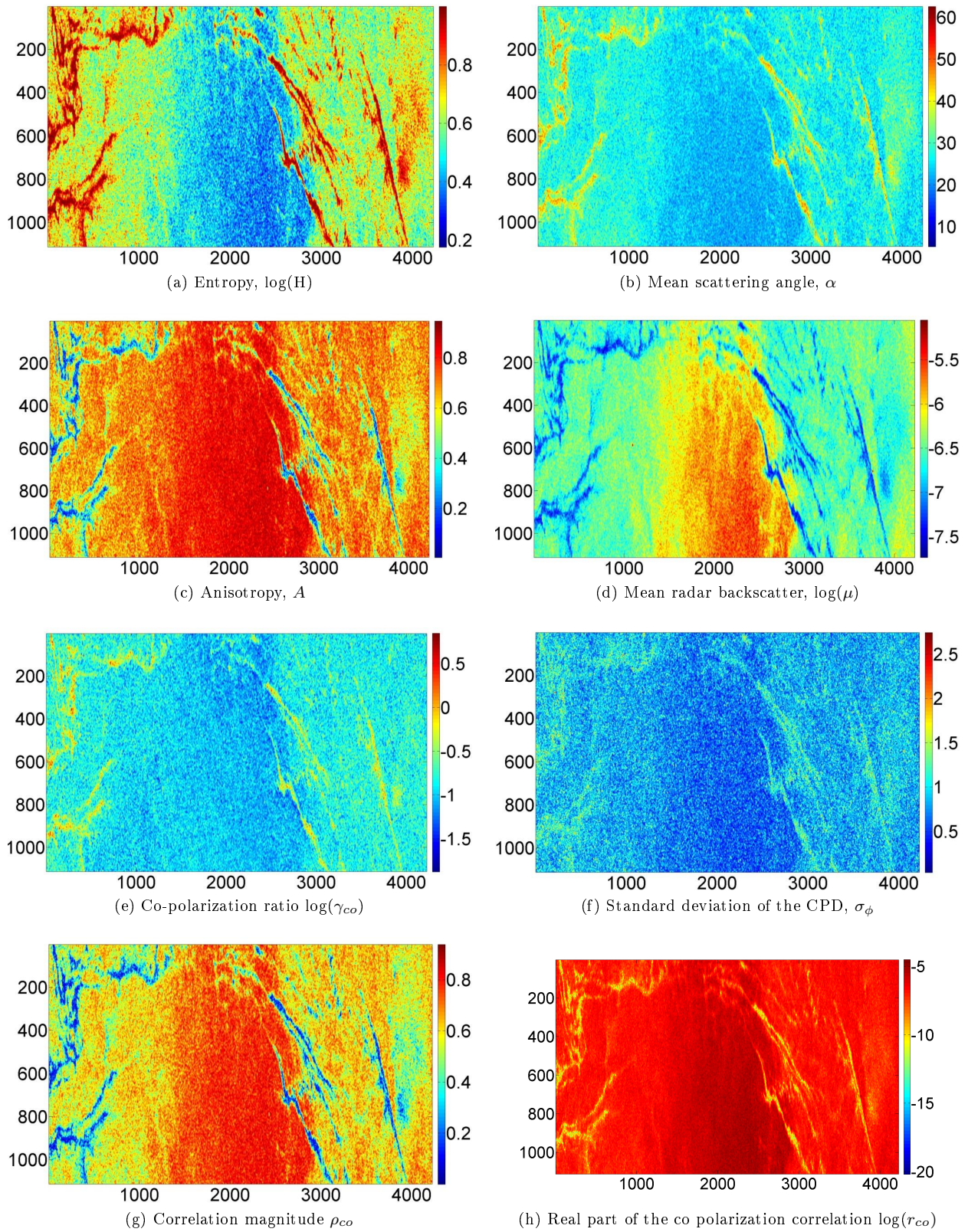


Figure 7.2: Multi-polarization features calculated from image #1

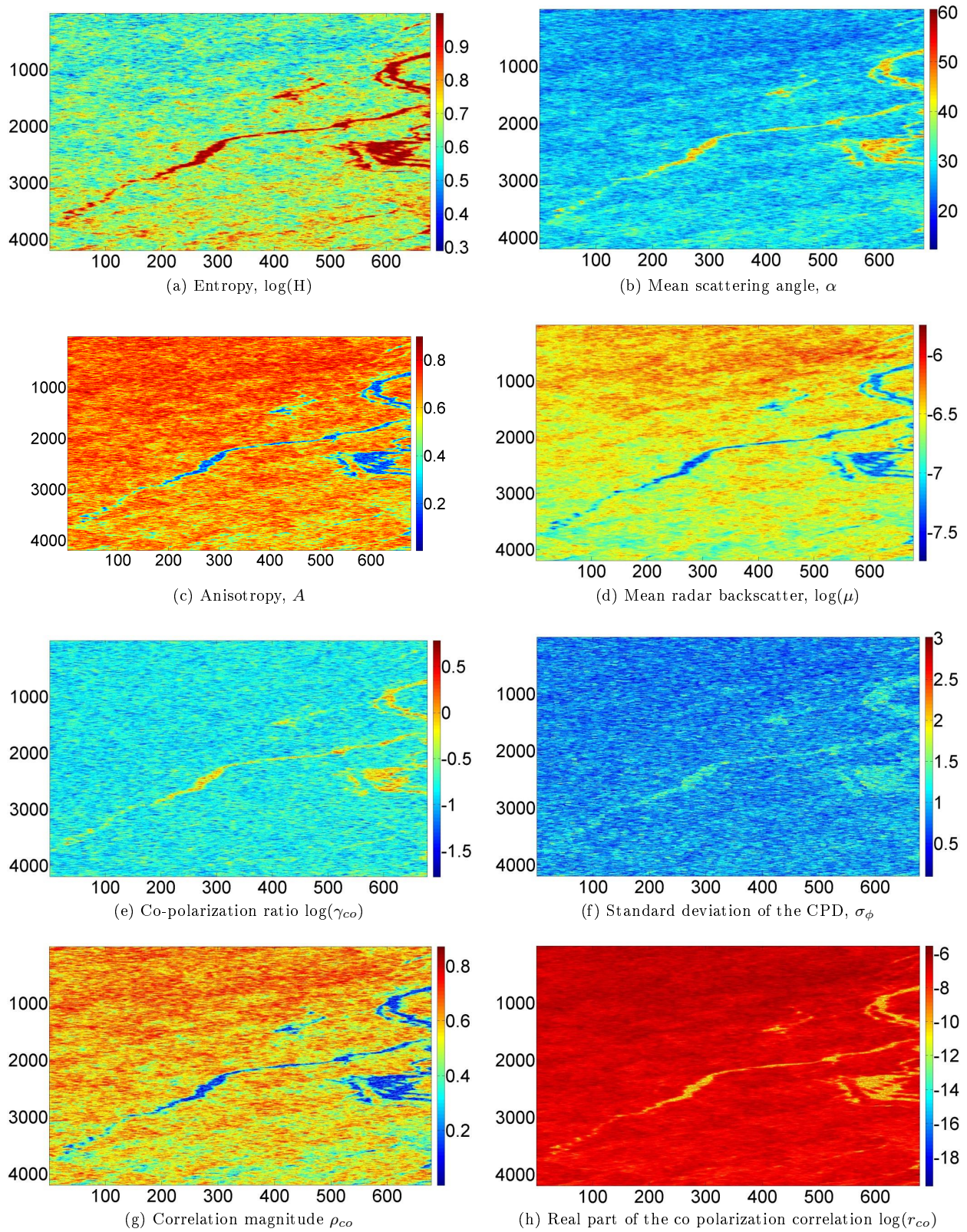


Figure 7.3: Multi-polarization features calculated from image #2

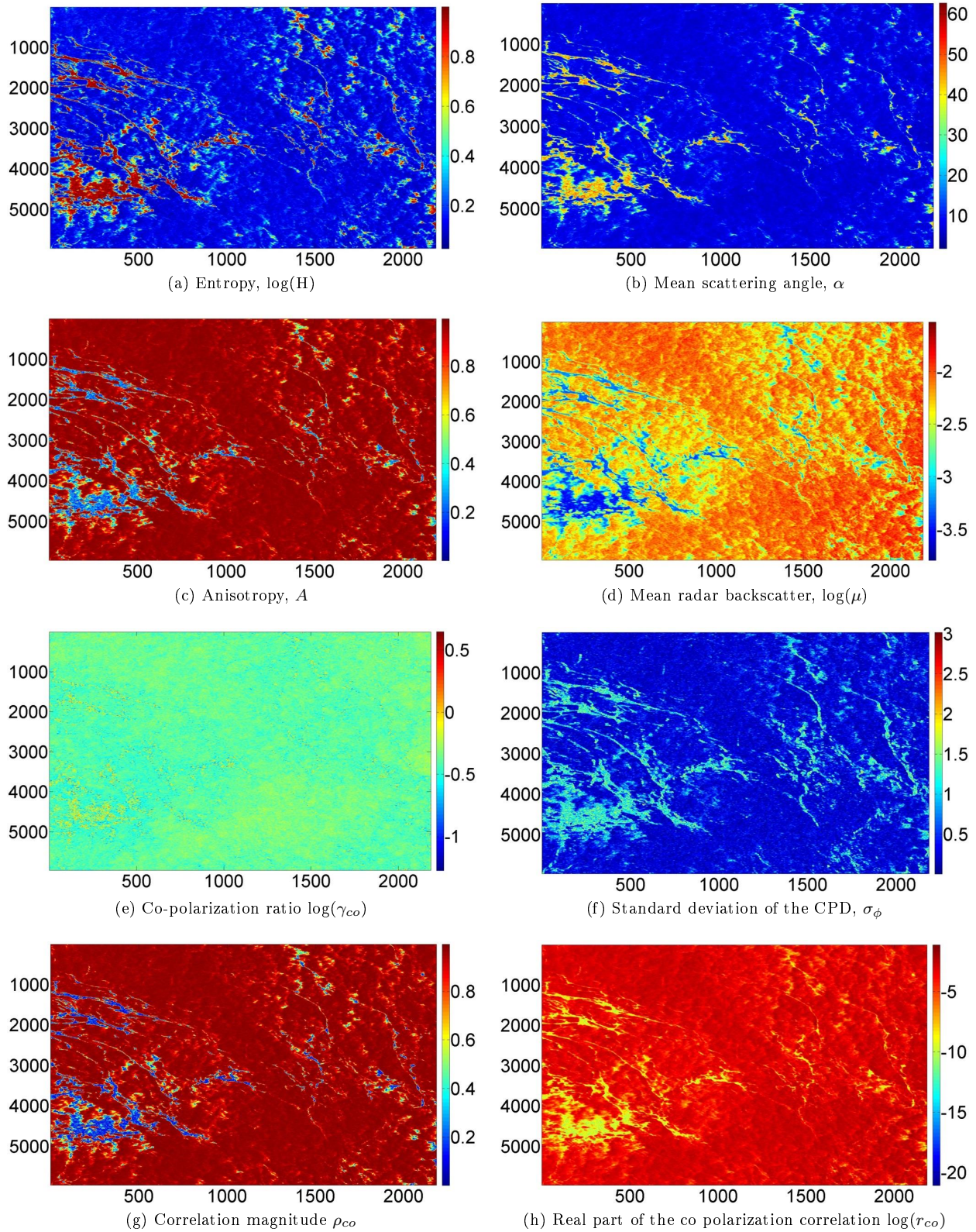


Figure 7.4: Multi-polarization features calculated from image #3

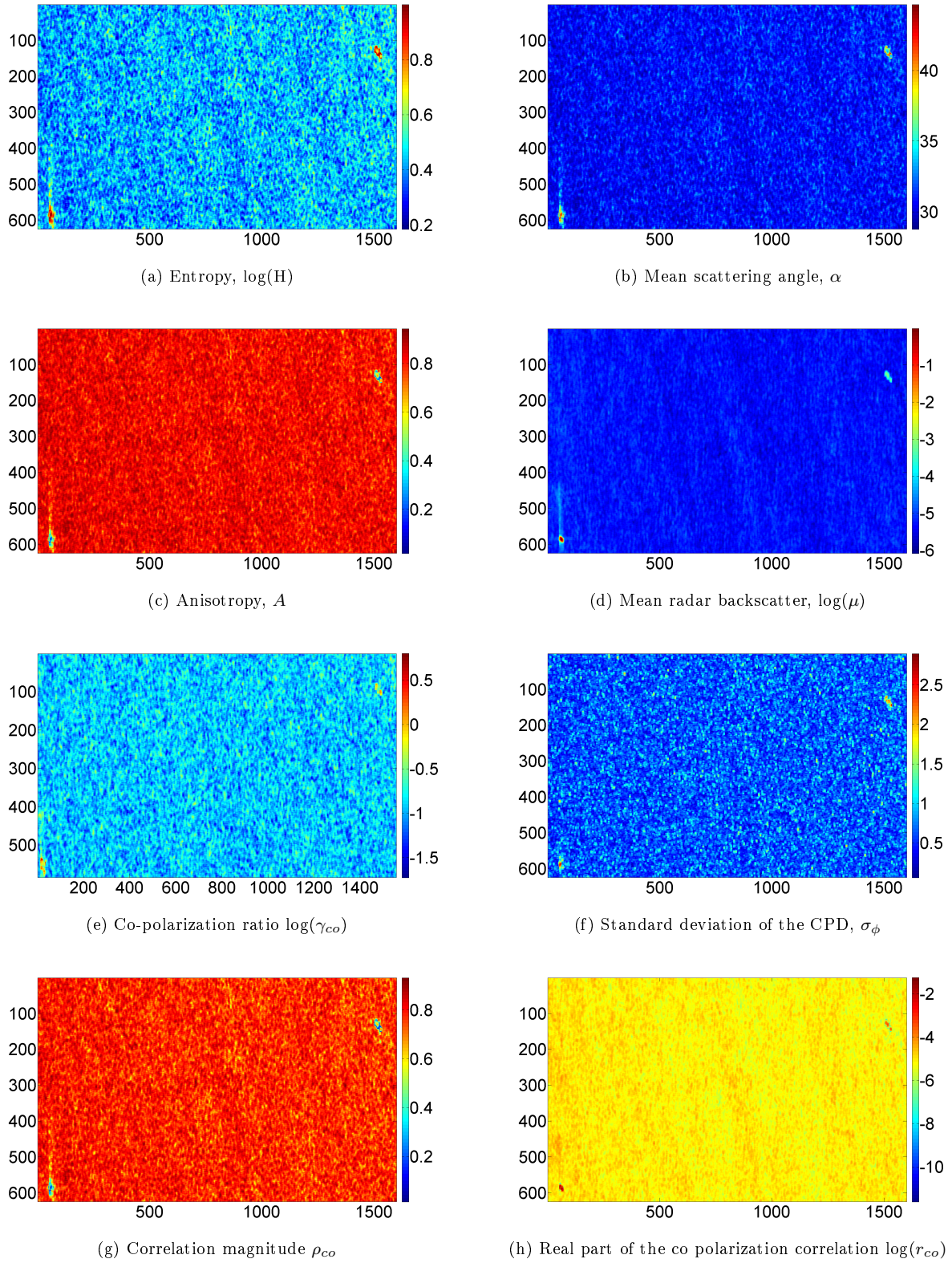


Figure 7.5: Multi-polarization features calculated from image #4

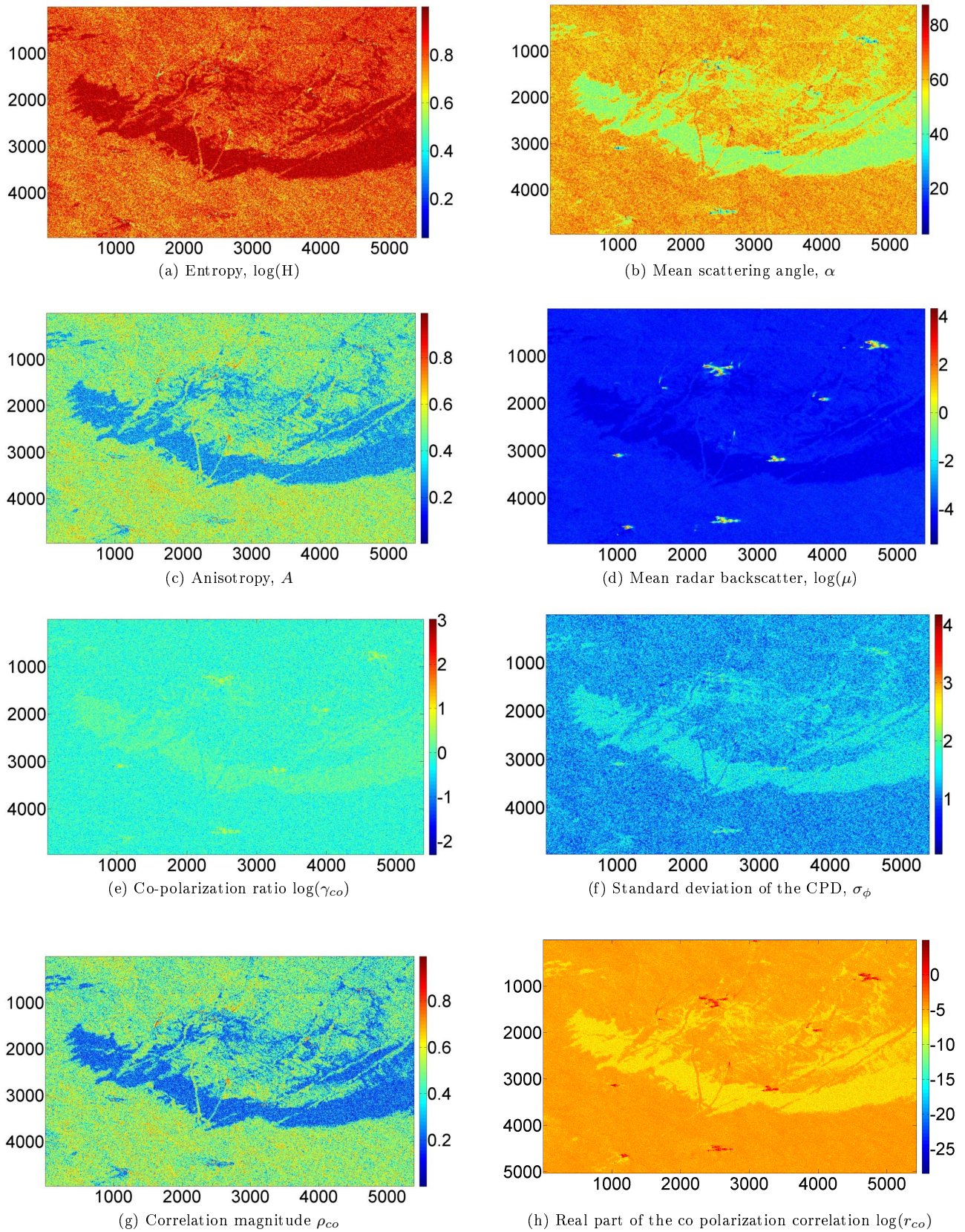
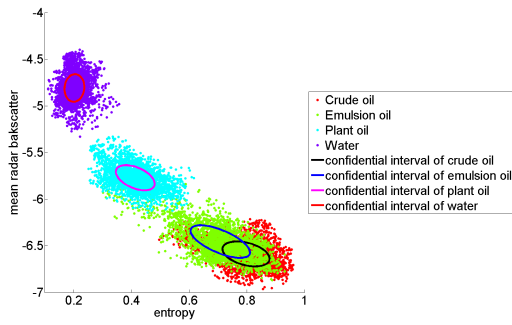
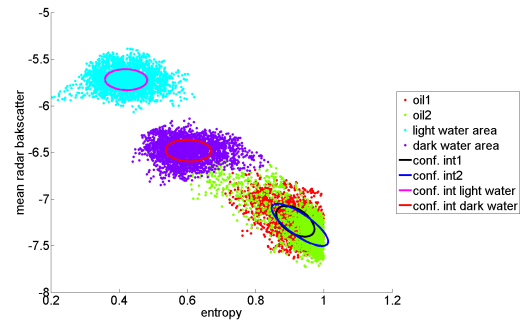


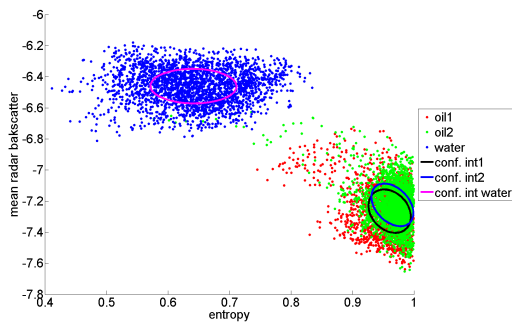
Figure 7.6: Multi-polarization features calculated from image #5



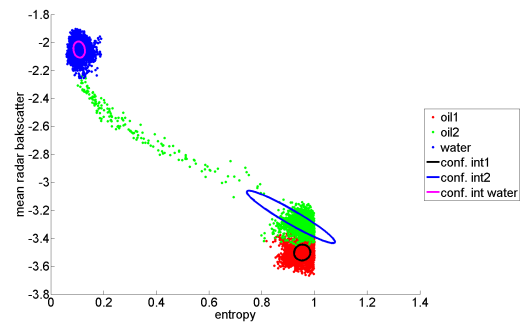
(a) Scatterplot from the OPV image



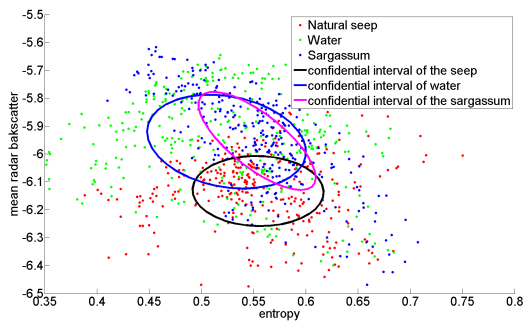
(b) Scatterplot from image #1



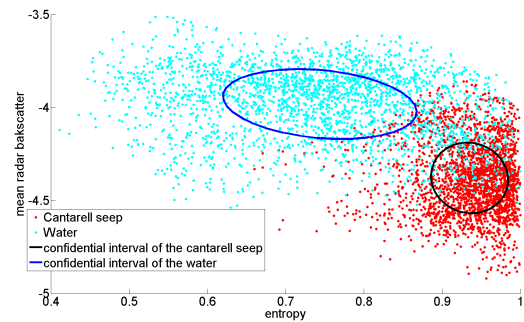
(c) Scatterplot from image #2



(d) Scatterplot from image #3

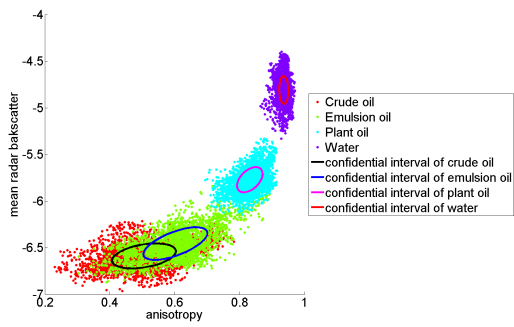


(e) Scatterplot from image #4

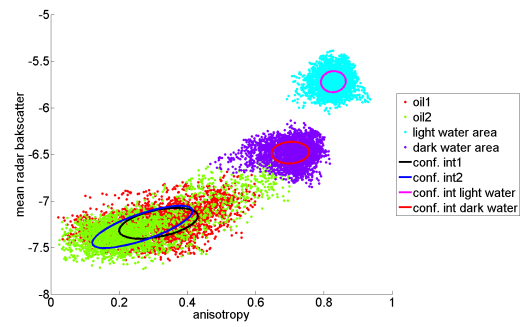


(f) Scatterplot from image #5

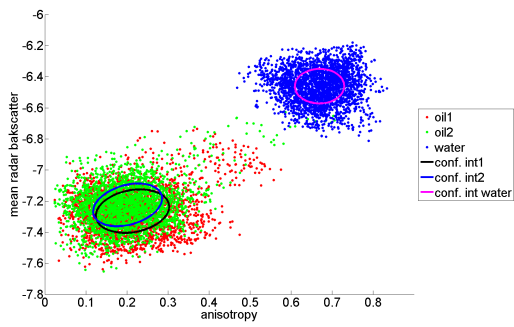
Figure 7.7: Scatter plots of the entropy vs. mean radar backscatter



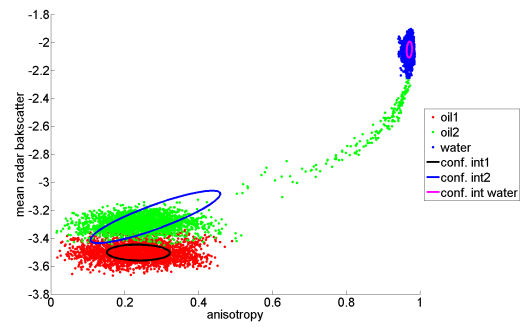
(a) Scatterplot from the OPV image



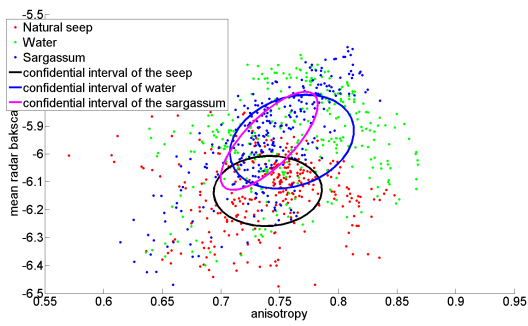
(b) Scatterplot from the #1 image



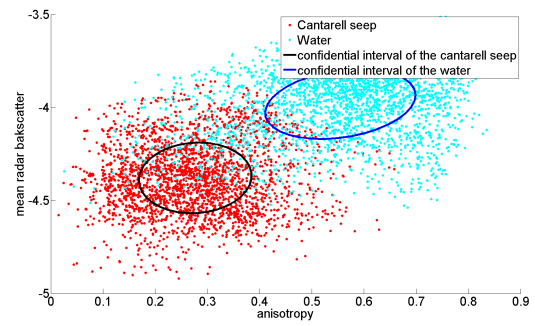
(c) Scatterplot from image #2 image



(d) Scatterplot from image #3 image

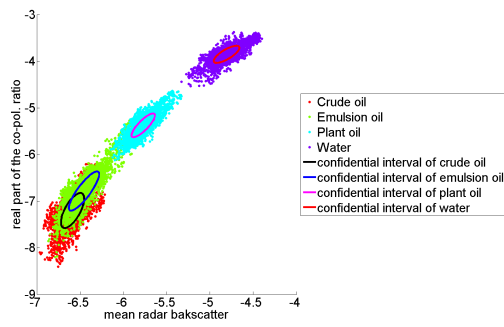


(e) Scatterplot from image #4 image

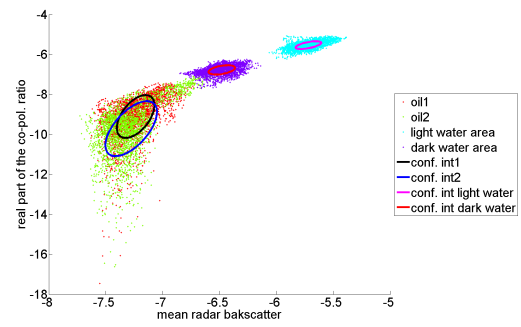


(f) Scatterplot from image #5 image

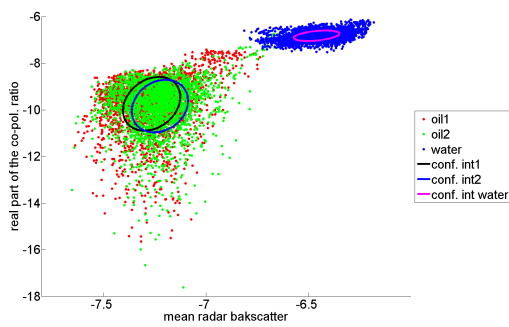
Figure 7.8: Scatter plots of the anisotropy vs. mean radar backscatter



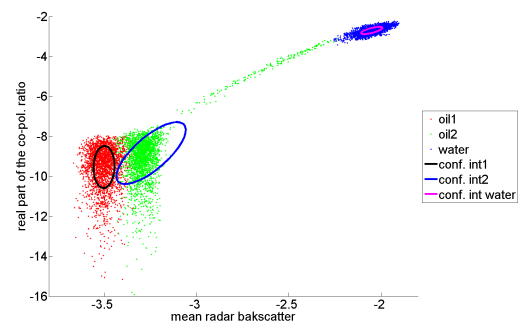
(a) Scatterplot from the OPV image



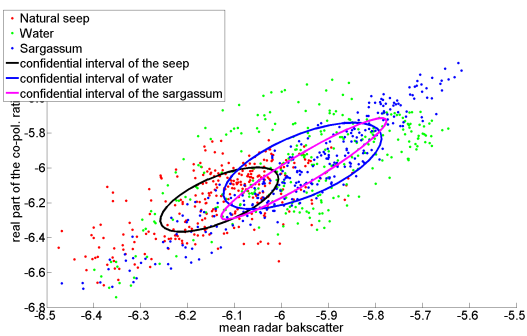
(b) Scatterplot from image #1



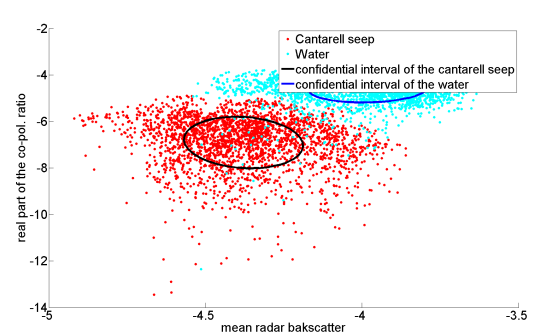
(c) Scatterplot from image #2



(d) Scatterplot from image #3

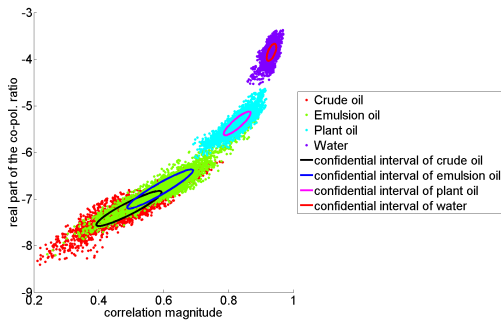


(e) Scatterplot from image #4

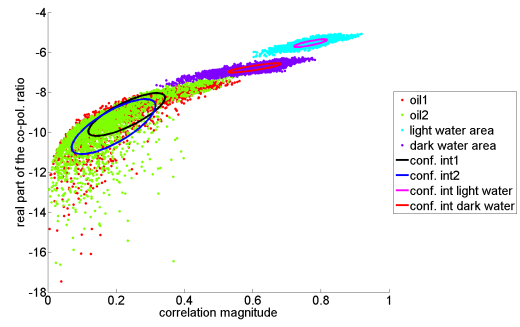


(f) Scatterplot from image #5

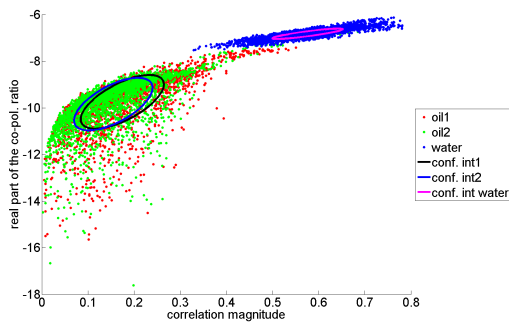
Figure 7.9: Scatter plots of the real part of the co-polarization ratio vs. mean radar backscatter



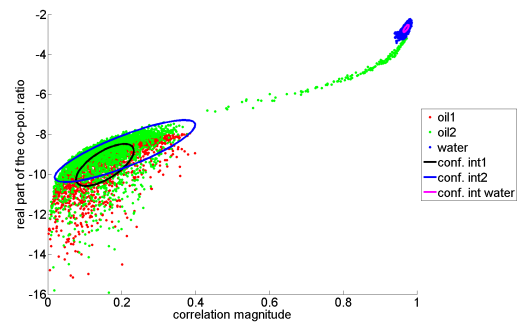
(a) Scatterplot from the OPV image



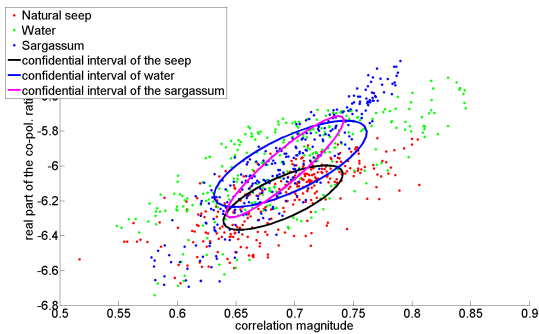
(b) Scatterplot from image #1



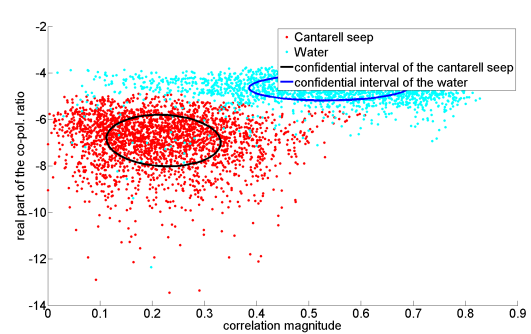
(c) Scatterplot from image #2



(d) Scatterplot from image #3

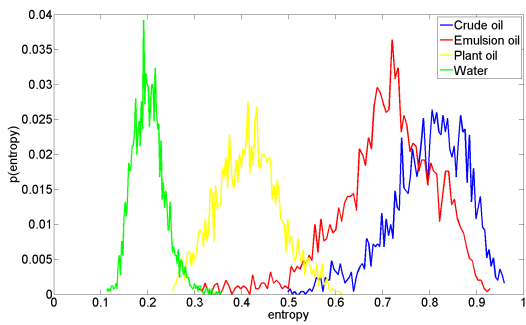


(e) Scatterplot from image #4

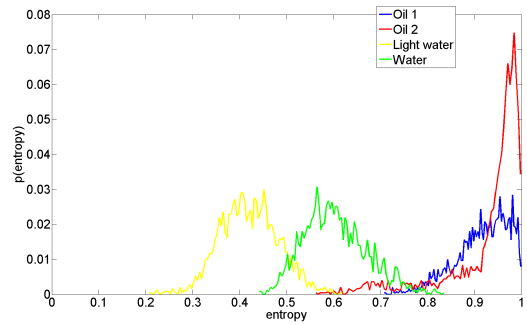


(f) Scatterplot from image #5

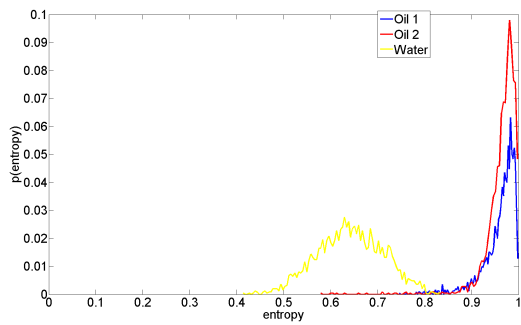
Figure 7.10: Scatter plots of the real part of the co-polarization ratio vs. correlation magnitude



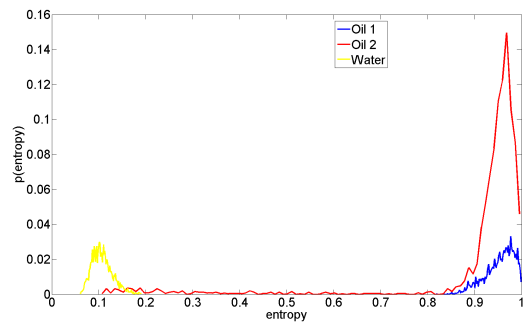
(a) Entropy of the OPV image



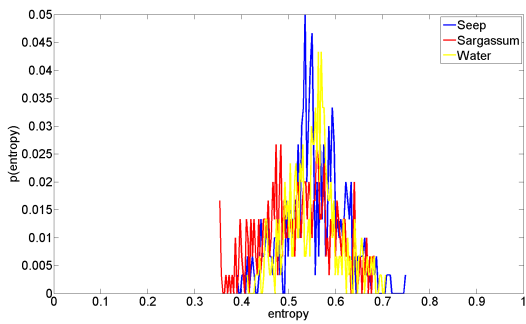
(b) Entropy of image #1



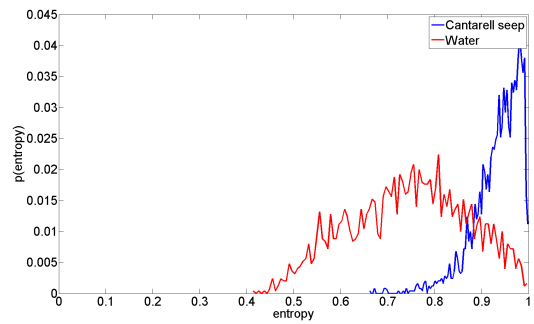
(c) Entropy of image #2



(d) Entropy of image #3

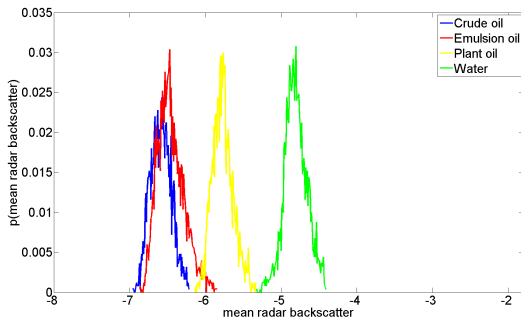


(e) Entropy of image #4

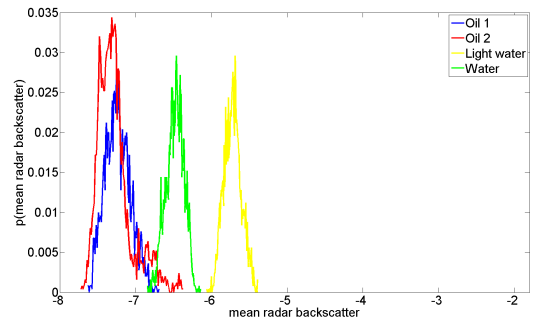


(f) Entropy of image #5

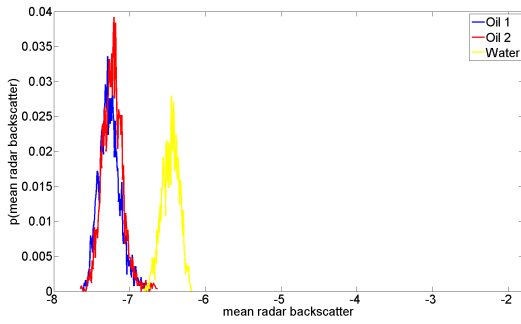
Figure 7.11: Histograms of the entropy from all the images



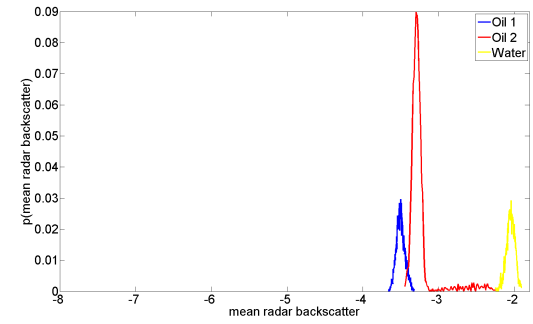
(a) Mean radar backscatter of the OPV image



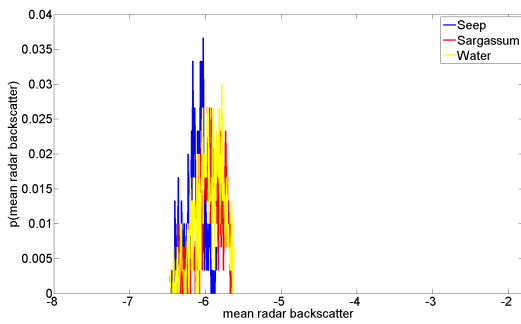
(b) Mean radar backscatter of image #1



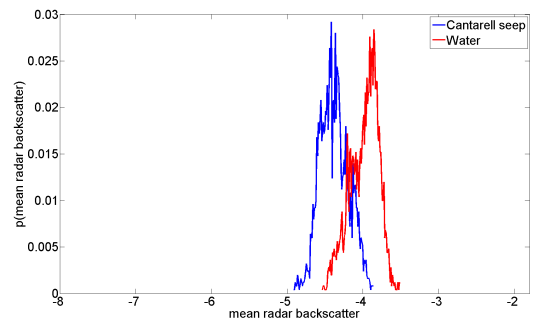
(c) Mean radar backscatter of image #2



(d) Mean radar backscatter of image #3

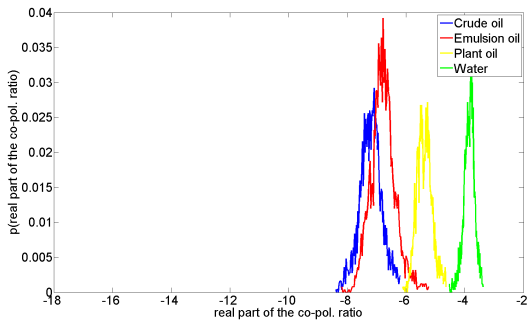


(e) Mean radar backscatter of image #4

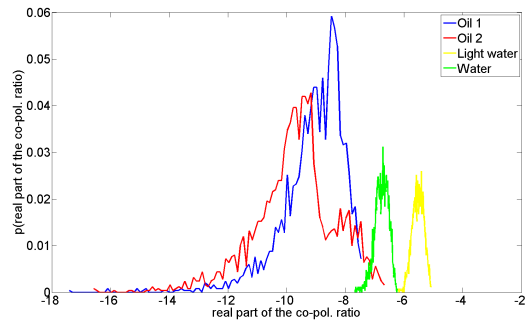


(f) Mean radar backscatter of image #5

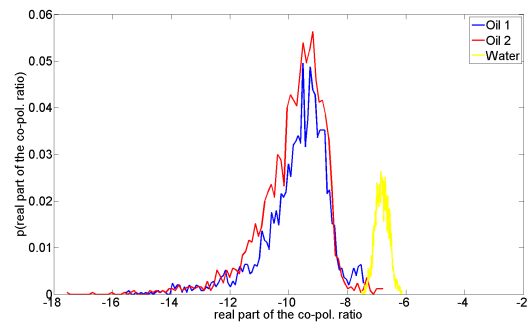
Figure 7.12: Histograms of the mean radar backscatter from all the images



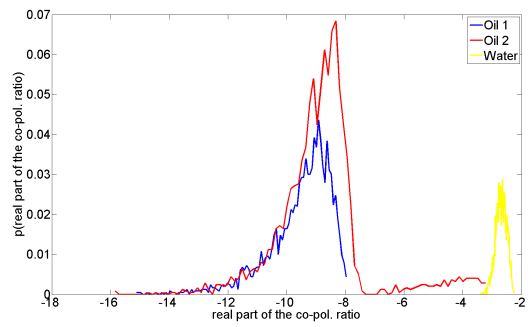
(a) Real part of the co-polarization ratio of the OPV image



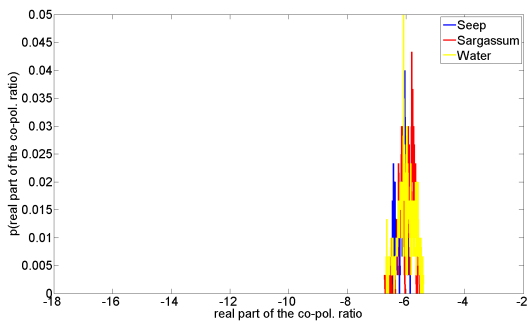
(b) Real part of the co-polarization ratio of image #1



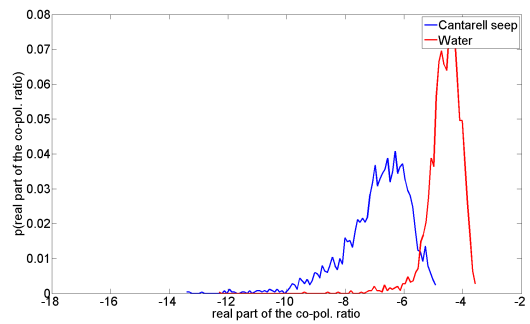
(c) Real part of the co-polarization ratio of image #2



(d) Real part of the co-polarization ratio of image #3

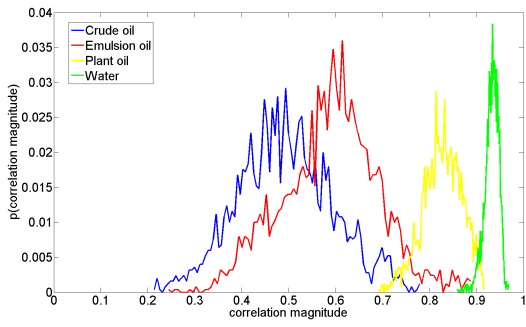


(e) Real part of the co-polarization ratio of image #4

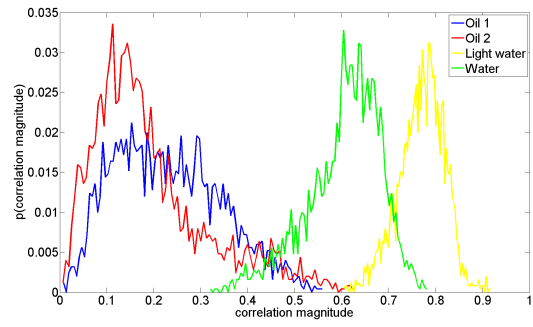


(f) Real part of the co-polarization ratio of image #5

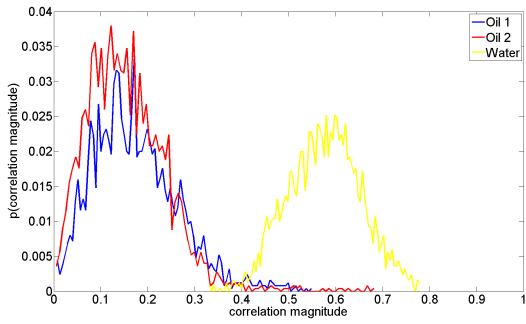
Figure 7.13: Histograms of the real part of the co-polarization ratio from all the images



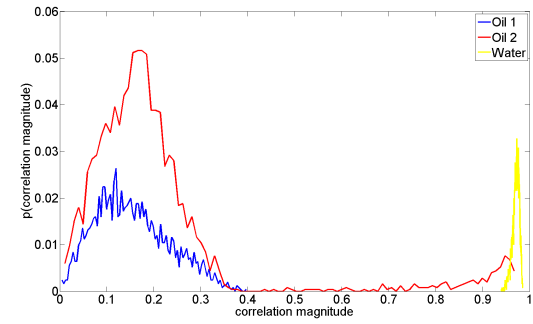
(a) Correlation magnitude of the OPV image



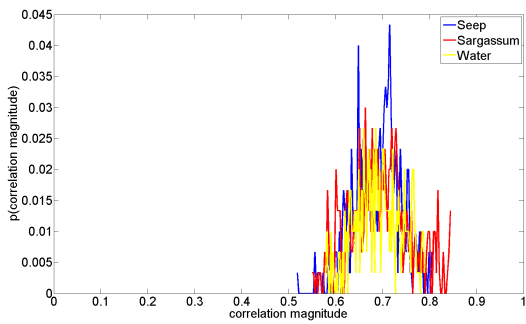
(b) Correlation magnitude #1 image



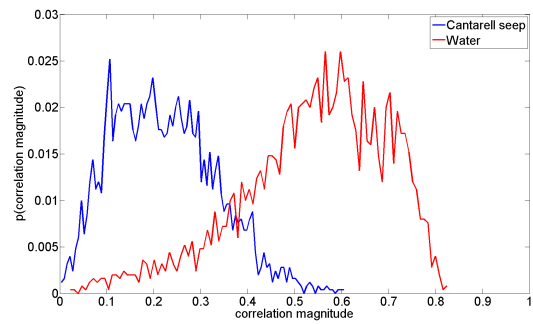
(c) Correlation magnitude of the #2 image



(d) Correlation magnitude of the #3 image

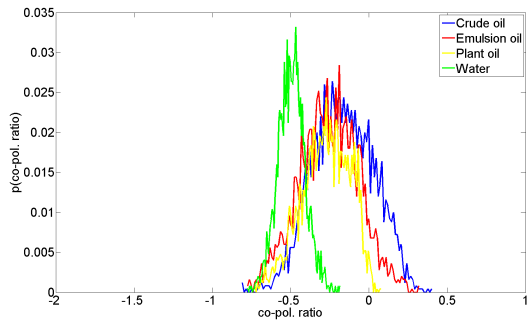


(e) Correlation magnitude of the #4 image

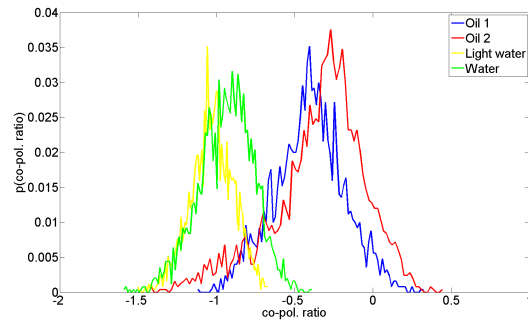


(f) Correlation magnitude of the #5 image

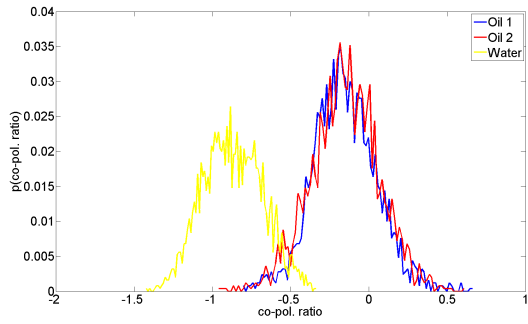
Figure 7.14: Histograms of the correlation magnitude from all the images



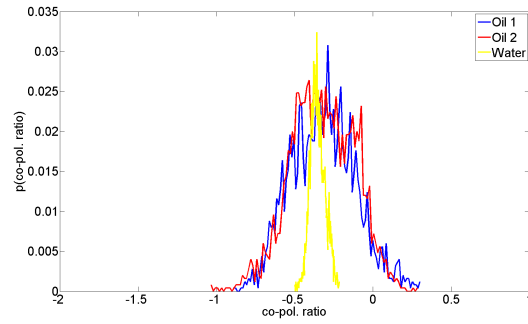
(a) Co-polarization ratio of the OPV image



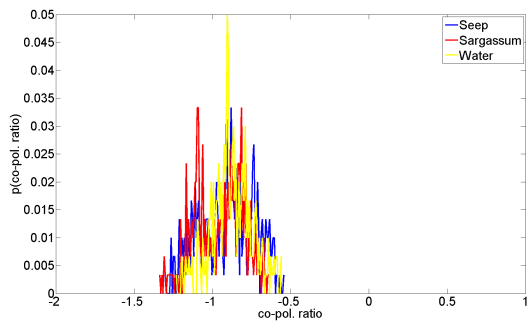
(b) Co-polarization ratio of image #1



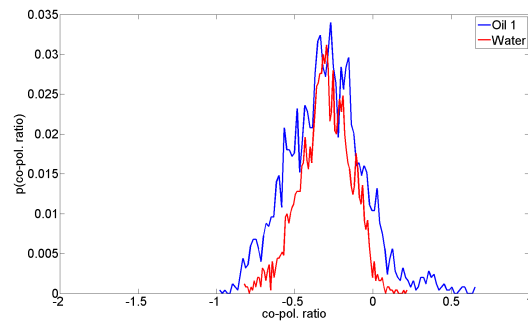
(c) Co-polarization ratio of image #2



(d) Co-polarization ratio of image #3

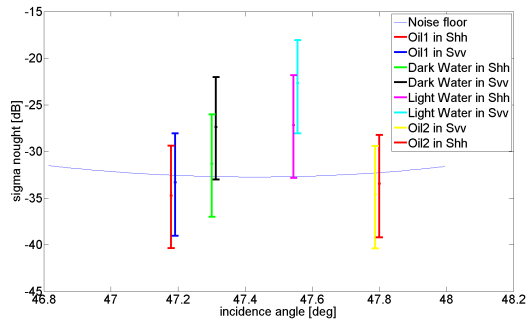


(e) Co-polarization ratio of image #4

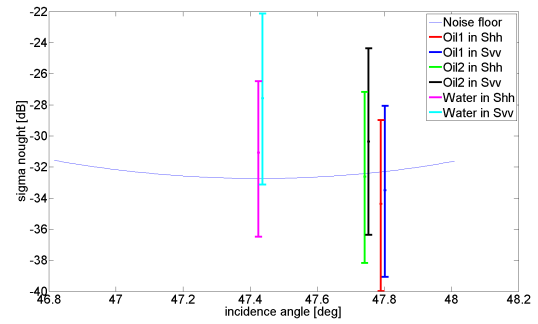


(f) Co-polarization ratio of image #5

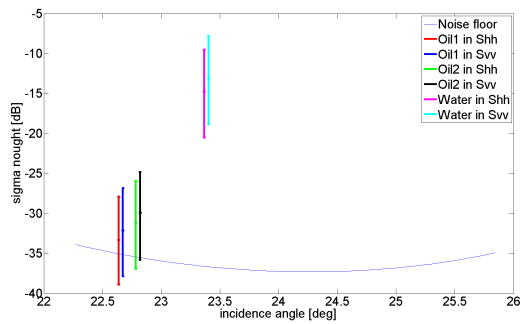
Figure 7.15: Histograms of the co-polarization ratio from all the images



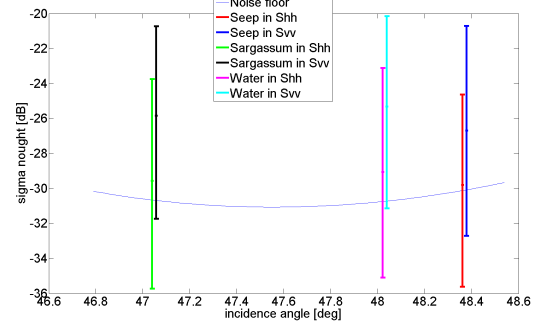
(a) Noise floor of image #1



(b) Noise floor of image #2

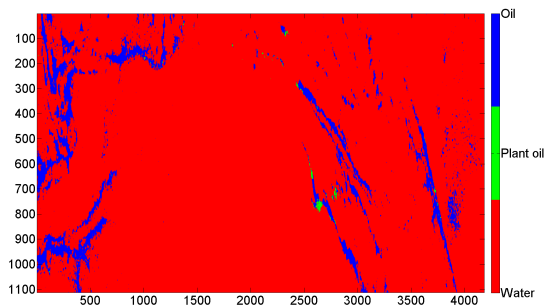


(c) Noise floor of image #3

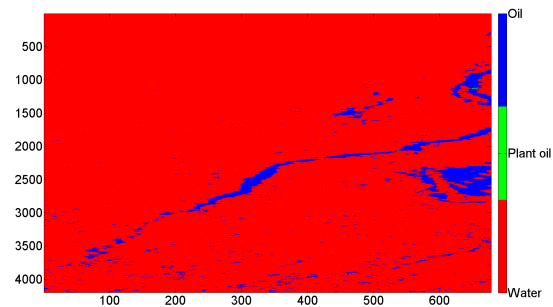


(d) Noise floor of image #4

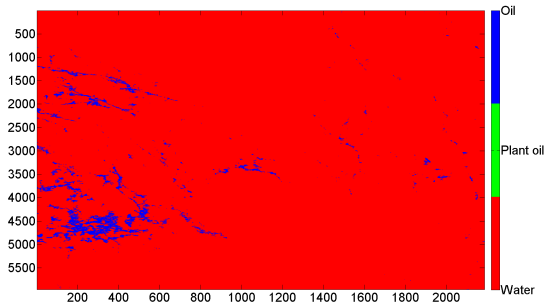
Figure 7.16: The noise floor plotted as a function of the incidence angle. Also the mean and standard deviation of the different patches from figure 6.1 are plotted with one deviation up, and one deviation down



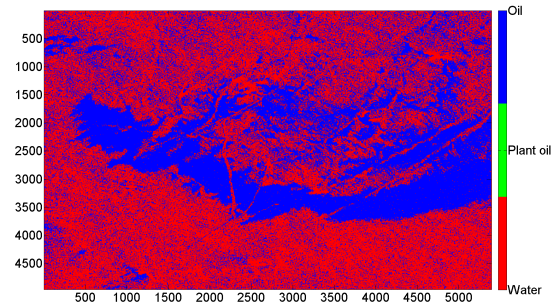
(a) Classification of image #1



(b) Classification of image #2

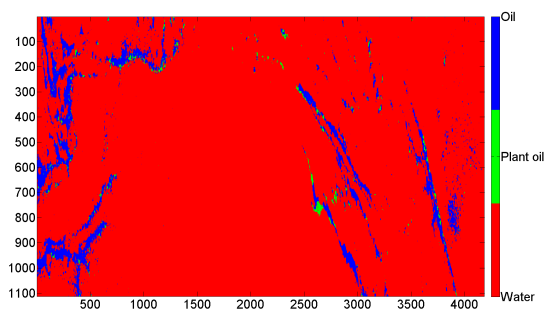


(c) Classification of image #3

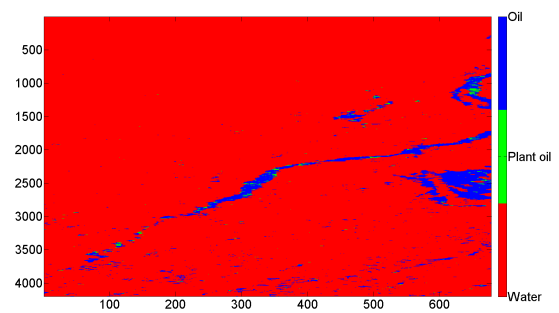


(d) Classification of image #5

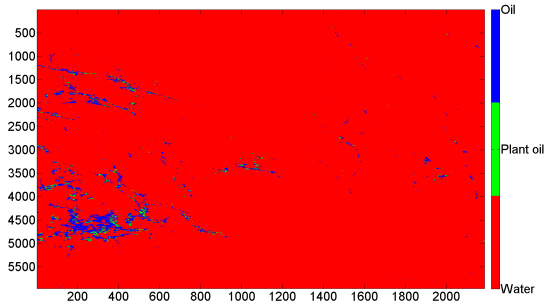
Figure 7.17: The Radarsat-2 scenes from the Gulf classified based on the mean radar backscatter feature vector



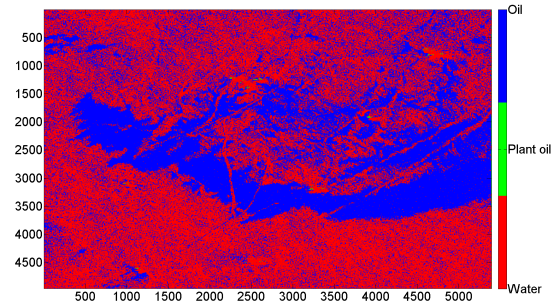
(a) Classification of image #1



(b) Classification of image #2



(c) Classification of image #3



(d) Classification of image #5

Figure 7.18: The Radarsat-2 scenes from the Gulf classified based the entropy feature vector

Chapter 8

Conclusion

In this thesis, different oil types in SAR-images have been studied. The intension was to investigate the ability of multi-polarization SAR to explore differences between natural seeps, biogenic slicks and crude-oil. Five quad-pol Radarsat-2 C-band images and one X-band dual-pol TerraSAR-X scene were used. Four of the Radarsat-2 images were from the Gulf of Mexico (#1, #2, #3 and #4), three with unknown dark patches and one that contained a seep and sargassum. The last Radarsat-2 image included both crude-oil, emulsion and plant oil (OPV-scene). The TerraSAR-X image (#5) contained the famous Cantarell seep. Most of the study have been about the OPV-scene and image #1, #2 and #3, while image #4 and #5 were used for comparison. A visual and statistical investigation of polarimetric features have been presented. A supervised classification was also executed to see if the dark patches would be stated as crude oil or plant oil.

First of all, eight different multi-polarimetric features were derived, studied and compared for all the scenes. Visually the features distinguish between the slicks and sea. The reason for this is the different scattering processes from different surface roughness and change in dielectric constant. The contrast between oil and sea varies, depending on the feature. In most of the features, the slicks from the Gulf showed similar properties as crude-oil. In summary, the entropy and the mean radar backscatter gives the best contrast between oil and water.

Secondly, histograms and scatterplots were made. They showed that slick covered areas made their own pdfs and clusters, separated from the water. The separability showed to be better in C-band than in X-band. Values from some of the figures showed that the seep-slicks have different values than the oil-values in the OPV-scene. A small problem though is that the differences between the seeps and the oil may be affected by the difference of incidence angle, wind speed and noise level between the scenes.

The classification used in this thesis showed that the dark patches from image #1, #2, #3 and #5 most probably are emulsion and crude-oil, rather than plant oil. Variations inside the slicks were observed from the classification too. The ML-algorithm show potential to classify seeps, but with only one image as training data the classification is not trustworthy enough.

Hence, for the dark patches in image #1, #2 and #3, they are assumed likely to be natural oil seeps because of the results and no sign of vessels or rigs. The seeps and crude-oil express some differences in most the multipolarimetric features, but to get more knowledge about these differences, a further investigation is needed where sea state, incidence angle and noise are more corrected for. Larger differences were observed between the seeps and plant-oil which can open the possibility that the features are able to discriminate between seeps and look-alikes.

8.1 Future work

Suggestions for future work:

- A problem for characterization of natural seeps is the lack of data and ground truth. More multi-polarization SAR-mages with observed seeps could help to study their polarimetric radar signature and the potential of inferring information about their physical and chemical properties. Images containing both seeps and biogenic slick could make a basis to compare seeps with look-alikes under the same weather conditions.
- Really interesting would be to study the same seeps with different bands (X, C and L). A comparison of seeps and how they behave in the different bands would give a good overview of which band is good for different purposes.
- A more advanced algorithm for segmentation and classification which is better trained with more data. Classification based on more than one feature would also be interesting.

Bibliography

- [1] B. Minchew, C. Jones, and B. Holt, "Polarimetric analysis of backscatter from the deepwater horizon oil spill using l-band synthetic aperture radar," *Geoscience and Remote Sensing, IEEE Transactions on*, vol. 50, no. 10, pp. 3812–3830, Oct.2012.
- [2] C. Brekke and A. Solberg, "Oil spill detection by satellite remote sensing," *Remote Sensing of Environment*, vol. 95, no. 1, pp. 1–13, 2005.
- [3] O. Garcia-Pineda, I. MacDonald, and B. Zimmer, "Synthetic aperture radar image processing using the supervised textural-neural network classification algorithm," in *Geoscience and Remote Sensing Symposium, 2008. IGARSS 2008. IEEE International*, vol. 4, pp. IV –1265 –IV –1268, july 2008.
- [4] Wikipedia, "Petroleum seep — wikipedia, the free encyclopedia," 2013. [Online; accessed 23-January-2013].
- [5] V. V. Zatyagalova, A. Y. Ivanov, and B. N. Golubov, "Application of envisat sar imagery for mapping and estimation of natural oil seeps in the south caspian sea," in *Proceedings of the Envisat symposium, Montreux, Switzerland (ESA SP-636, 2007*.
- [6] K. Kvenvolden and C. Cooper, "Natural seepage of crude oil into the marine environment," *Geo-Marine Letters*, vol. 23, no. 3, pp. 140–146, 2003.
- [7] N. Bartsch, K. Gruner, W. Keydel, and F. Witte, "Contributions to oil-spill detection and analysis with radar and microwave radiometry: Results of the archimedes ii campaign," *Geoscience and Remote Sensing, IEEE Transactions on*, vol. GE-25, pp. 677 –690, nov. 1987.
- [8] K. Bjerde, A. Solberg, and R. Solberg, "Oil spill detection in sar imagery," in *Geoscience and Remote Sensing Symposium, 1993. IGARSS '93. Better Understanding of Earth Environment., International*, pp. 943 –945 vol.3, aug 1993.
- [9] M. Marghany, "Finite element model of residual currents and oil spills transport," in *Geoscience and Remote Sensing Symposium, 2000. Proceedings. IGARSS 2000. IEEE 2000 International*, vol. 7, pp. 2966 –2968 vol.7, 2000.
- [10] F. Girard-Arduin, G. Mercier, F. Collard, and R. Garello, "Operational oil-slick characterization by sar imagery and synergistic data," *Oceanic Engineering, IEEE Journal of*, vol. 30, no. 3, pp. 487–495, 2005.
- [11] W. Tian, Y. Shao, J. Yuan, S. Wang, and Y. Liu, "An experiment for oil spill recognition using radarsat-2 image," in *Geoscience and Remote Sensing Symposium (IGARSS), 2010 IEEE International*, pp. 2761–2764, 2010.
- [12] F. Zhang, Y. Shao, W. Tian, and S. Wang, "Oil spill identification based on textural information of sar image," in *Geoscience and Remote Sensing Symposium, 2008. IGARSS 2008. IEEE International*, vol. 4, pp. IV –1308 –IV –1311, july 2008.
- [13] A. H. S. Solberg, C. Brekke, and P. O. Husoy, "Oil spill detection in radarsat and envisat sar images," *Geoscience and Remote Sensing, IEEE Transactions on*, vol. 45, pp. 746 –755, march 2007.

- [14] S. Singha, T. Bellerby, and O. Trieschmann, "Detection and classification of oil spill and look-alike spots from sar imagery using an artificial neural network," in *Geoscience and Remote Sensing Symposium (IGARSS), 2012 IEEE International*, pp. 5630–5633, 2012.
- [15] M. Marghany and M. Hashim, "Comparative algorithms for automatic detection of oil spill in multisar of radarsat-1 sar and envisat data," in *Signal and Image Processing Applications (ICSIPA), 2011 IEEE International Conference on*, pp. 559–562, 2011.
- [16] P. Liu and C. Zhao, "Oil spill identification in marine sar images based on texture feature and fuzzy logic system," in *Fuzzy Systems and Knowledge Discovery, 2009. FSKD '09. Sixth International Conference on*, vol. 3, pp. 433–437, 2009.
- [17] A. H. S. Solberg, C. Brekke, and P. Ove Husoy, "Oil spill detection in radarsat and envisat sar images," *Geoscience and Remote Sensing, IEEE Transactions on*, vol. 45, no. 3, pp. 746–755, 2007.
- [18] M. Migliaccio, A. Gambardella, and M. Tranfaglia, "Sar polarimetry to observe oil spills," *Geoscience and Remote Sensing, IEEE Transactions on*, vol. 45, no. 2, pp. 506–511, 2007.
- [19] B. Zhang, W. Perrie, X. Li, and W. G. Pichel, "Mapping sea surface oil slicks using radarsat-2 quad-polarization sar image," *Geophysical research letters*, vol. 38, no. 10, p. L10602, 2011.
- [20] S. Skrunes, C. Brekke, and T. Eltoft, "Ocean surface slick characterization by multi-polarization radarsat-2 data," in *SPIE Remote Sensing*, pp. 85360Q–85360Q, International Society for Optics and Photonics, 2012.
- [21] S. Skrunes, C. Brekke, and T. Eltoft, "An experimental study on oil spill characterization by multi-polarization sar," *Synthetic Aperture Radar, 2012. EUSAR. 9th European Conference on*, pp. 139–142, april 2012.
- [22] S. Skrunes, C. Brekke, and T. Eltoft, "Oil spill characterization with multi-polarization c- and x-band sar," in *Geoscience and Remote Sensing Symposium (IGARSS), 2012 IEEE International*, pp. 5117–5120, july 2012.
- [23] J. Lee and E. Pottier, *Polarimetric Radar Imaging: From Basics to Applications*. Optical Science and Engineering, Taylor & Francis, 2009.
- [24] J. van Zyl, *Synthetic Aperture Radar Polarimetry*. JPL Space Science and Technology Series, John Wiley & Sons, 2011.
- [25] R. Shirvany, *Estimation of the Degree of Polarization in Polarimetric SAR Imagery: Principles and Applications*. PhD thesis, 2012.
- [26] J.-S. Lee, M. Grunes, and E. Pottier, "Quantitative comparison of classification capability: fully polarimetric versus dual and single-polarization sar," *Geoscience and Remote Sensing, IEEE Transactions on*, vol. 39, no. 11, pp. 2343–2351, 2001.
- [27] F. Girard-Arduin, G. Mercier, and R. Garello, "Oil slick detection by sar imagery: potential and limitation," in *OCEANS 2003. Proceedings*, vol. 1, pp. 164–169, IEEE, 2003.
- [28] S. N. Anfinsen, *Statistical analysis of multilook polarimetric radar images with the Mellin transform*. Universitetet i Tromsø, 2010.
- [29] T. Eltoft, "The rician inverse gaussian distribution: a new model for non-rayleigh signal amplitude statistics," *Image Processing, IEEE Transactions on*, vol. 14, no. 11, pp. 1722–1735, 2005.
- [30] D. Santosh, V. Kumar, D. Ramesh, and P. Prasad, "Efficient techniques for denoising of speckle and highly corrupted impulse noise images," in *Electronics Computer Technology (ICECT), 2011 3rd International Conference on*, vol. 3, pp. 253–257, 2011.

- [31] C. Lopez-Martinez and E. Pottier, "On the extension of multidimensional speckle noise model from single-look to multilook sar imagery," *Geoscience and Remote Sensing, IEEE Transactions on*, vol. 45, no. 2, pp. 305–320, 2007.
- [32] Y. Jiang, X. Wang, X. Xu, and X. Ye, "Speckle noise filtering for sea sar image," in *Intelligent Systems, 2009. GCIS '09. WRI Global Congress on*, vol. 4, pp. 523–527, 2009.
- [33] Wikipedia, "Envisat — wikipedia, the free encyclopedia," 2013. [Online; accessed 4-April-2013].
- [34] C. Brekke and A. H. S. Solberg, "Classifiers and confidence estimation for oil spill detection in envisat asar images," *Geoscience and Remote Sensing Letters, IEEE*, vol. 5, no. 1, pp. 65–69, 2008.
- [35] W. Tian, Y. Shao, and S. Wang, "A system for automatic identification of oil spill in envisat asar images," in *Geoscience and Remote Sensing Symposium, 2008. IGARSS 2008. IEEE International*, vol. 3, pp. III – 1394–III – 1397, 2008.
- [36] Wikipedia, "Terrasar-x — wikipedia, the free encyclopedia," 2013. [Online; accessed 4-April-2013].
- [37] F. Nunziata, A. Montuori, and M. Migliaccio, "Dual-polarized cosmo skymed sar data to observe metallic targets at sea," in *Geoscience and Remote Sensing Symposium (IGARSS), 2011 IEEE International*, pp. 2270–2273, 2011.
- [38] C. Livingstone, I. Sikaneta, C. Gierull, S. Chiu, and P. Beaulne, "Radarsat-2 system and mode description," tech. rep., DTIC Document, 2006.
- [39] P. Clemente-Colón and X.-H. Yan, "Low-backscatter ocean features in synthetic aperture radar imagery," *Johns hopkins APL technical digest*, vol. 21, no. 1, pp. 116–121, 2000.
- [40] T. Wahl, Å. Skøelv, J. P. Pedersen, L.-G. Seljelv, J. H. Andersen, O. A. Follum, T. Anderssen, G. D. Strøm, T.-I. Bern, H. H. Espedal, *et al.*, "Radar satellites: A new tool for pollution monitoring in coastal waters," *Coastal management*, vol. 24, no. 1, pp. 61–71, 1996.
- [41] W. Alpers and H. Hühnerfuss, "The damping of ocean waves by surface films: A new look at an old problem," *Journal of Geophysical Research: Oceans (1978–2012)*, vol. 94, no. C5, pp. 6251–6265, 1989.
- [42] W. Alpers and H. Hühnerfuss, "Radar signatures of oil films floating on the sea surface and the marangoni effect," *Journal of Geophysical Research: Oceans (1978–2012)*, vol. 93, no. C4, pp. 3642–3648, 1988.
- [43] H. Hühnerfuss, W. Alpers, and W. L. Jones, "Measurements at 13.9 ghz of the radar backscattering cross section of the north sea covered with an artificial surface film," *Radio Science*, vol. 13, no. 6, pp. 979–983, 1978.
- [44] H. Hühnerfuss, W. Alpers, A. Cross, W. D. Garrett, W. C. Keller, P. A. Lange, W. J. Plant, F. Schlude, and D. L. Schuler, "The modification of x and l band radar signals by monomolecular sea slicks," *Journal of Geophysical Research: Oceans (1978–2012)*, vol. 88, no. C14, pp. 9817–9822, 1983.
- [45] A. Solberg, "Remote sensing of ocean oil-spill pollution," *Proceedings of the IEEE*, vol. 100, pp. 2931 –2945, oct. 2012.
- [46] M. Gade, J. Scholz, and C. von Viebahn, "On the detectability of marine oil pollution in european marginal waters by means of ers sar imagery," in *Geoscience and Remote Sensing Symposium, 2000. Proceedings. IGARSS 2000. IEEE 2000 International*, vol. 6, pp. 2510–2512 vol.6, 2000.
- [47] C. Jackson, J. Apel, and U. S. D. of Commerce, *Synthetic Aperture Radar: Marine User's Manual*. U.S. Department of Commerce, National Oceanic and Atmospheric Administration, 2004.

- [48] G. R. Valenzuela, "Theories for the interaction of electromagnetic and oceanic waves-a review," *Boundary-Layer Meteorology*, vol. 13, no. 1-4, pp. 61–85, 1978.
- [49] C. Brekke and F. forskningsinstitutt, *Automatic Screening of Synthetic Aperture Radar Imagery for Detection of Oil Pollution in the Marine Environment*. Series of dissertations submitted to the Faculty of Mathematics and Natural Sciences, University of Oslo, Department of Informatics, Faculty of Mathematics and Natural Science[s], University of Oslo, 2008.
- [50] F. Committee on Oil in the Sea: Inputs and N. R. C. Effects, *Oil in the Sea III:Inputs, Fates, and Effects*. The National Academies Press, 2003.
- [51] M. F. Fingas, "Studies on the evaporation regulation mechanisms of crude oil and petroleum products," *Advances in Chemical Engineering and Science*, vol. 2, no. 2, pp. 246–256, 2012.
- [52] V. Klemas, "Tracking and monitoring oil slicks using remote sensing," in *Baltic International Symposium (BALTIC), 2012 IEEE/OES*, pp. 1–7, 2012.
- [53] H. Dave, S. Mazumder, J. Samal, K. Pangtey, and D. Mitra, "Detection of natural hydrocarbon seepages using sar technology and associated subsurface studies in offshore mahanadi basin for delineation of possible areas of hydrocarbon exploration," in *Proceedings of the 2nd South Asian Geoscience Conference and Exhibition*, 2011.
- [54] Wikipedia, "Petroleum seep — wikipedia, the free encyclopedia," 2013. [Online; accessed 31-May-2013].
- [55] M. Wettle, P. Daniel, G. A. Logan, and M. Thankappan, "Offshore petroleum exploration from space: A developing capability at geoscience australia," in *OCEANS 2010 IEEE - Sydney*, pp. 1–7, 2010.
- [56] I. Leifer and I. MacDonald, "Dynamics of the gas flux from shallow gas hydrate deposits: interaction between oily hydrate bubbles and the oceanic environment," *Earth and Planetary Science Letters*, vol. 210, no. 3, pp. 411–424, 2003.
- [57] E. A. Solomon, M. Kastner, I. R. MacDonald, and I. Leifer, "Considerable methane fluxes to the atmosphere from hydrocarbon seeps in the gulf of mexico," *Nature Geoscience*, vol. 2, no. 8, pp. 561–565, 2009.
- [58] I. R. MacDonald, I. Leifer, R. Sassen, P. Stine, R. Mitchell, and N. Guinasso, "Transfer of hydrocarbons from natural seeps to the water column and atmosphere," *Geofluids*, vol. 2, no. 2, pp. 95–107, 2002.
- [59] O. Garcia-Pineda, B. Zimmer, M. Howard, W. Pichel, X. Li, and I. MacDonald, "Using sar images to delineate ocean oil slicks with a texture-classifying neural network algorithm (tcnna)," *Canadian Journal of Remote Sensing*, vol. 35, no. 5, pp. 411–421, 2009.
- [60] M. Rodriguez, K. Bannerman, R. Caceres, F. De Miranda, and E. Pedroso, "Cantarell natural seep modelling using sar derived ocean surface wind and meteo- oceanographic buoy data.," in *Geoscience and Remote Sensing Symposium, 2007. IGARSS 2007. IEEE International*, pp. 3257–3260, 2007.
- [61] A. Quintero-Marmol, E. Pedroso, C. Beisl, R. Caceres, F. De Miranda, K. Bannerman, P. Welgan, and O. Castillo, "Operational applications of radarsat-1 for the monitoring of natural oil seeps in the south gulf of mexico," in *Geoscience and Remote Sensing Symposium, 2003. IGARSS '03. Proceedings. 2003 IEEE International*, vol. 4, pp. 2744–2746 vol.4, 2003.
- [62] F. Pellon de Miranda, A. M. Q. Marmol, E. C. Pedroso, C. H. Beisl, P. Welgan, and L. M. Morales, "Analysis of radarsat-1 data for offshore monitoring activities in the cantarell complex, gulf of mexico, using the unsupervised semivariogram textural classifier (ustc)," *Canadian Journal of Remote Sensing*, vol. 30, no. 3, pp. 424–436, 2004.

- [63] E. Pedroso, F. De Miranda, K. Bannerman, C. HenriqueBeisl, M. Rodriguez, and R. Caceres, "A multi-sensor approach and ranking analysis procedure for oil seeps detection in marine environments," in *Geoscience and Remote Sensing Symposium, 2007. IGARSS 2007. IEEE International*, pp. 865–870, 2007.
- [64] M. Thankappan, G. Logan, M. Wettle, S. Reddy, and A. Jones, "Evaluation of terrasars-x for natural oil seep studies," in *ESA Special Publication*, vol. 668, p. 56, 2009.
- [65] N. D. B. Center, 2012. [Online; accessed 10-Desember-2012].
- [66] E. S. Agency, 2013. [Online; accessed 29-May-2013].
- [67] R. Polarimetry, "Advanced radar polarimetry tutorial,"
- [68] M. Migliaccio, F. Nunziata, and A. Gambardella, "On the co?polarized phase difference for oil spill observation," *International Journal of Remote Sensing*, vol. 30, no. 6, pp. 1587–1602, 2009.
- [69] F. Ulaby, K. Sarabandi, and A. Nashashibi, "Statistical properties of the mueller matrix of distributed targets," in *Radar and Signal Processing, IEE Proceedings F*, vol. 139, pp. 136–146, IET, 1992.
- [70] D. Velotto, M. Migliaccio, F. Nunziata, and S. Lehner, "Dual-polarized terrasars-x data for oil-spill observation," *Geoscience and Remote Sensing, IEEE Transactions on*, vol. 49, no. 12, pp. 4751–4762, 2011.
- [71] R. O. Duda, P. E. Hart, and D. G. Stork, *Pattern classification*. Wiley-interscience, 2012.
- [72] D. Kasilingam, D. Schuler, J.-S. Lee, and S. Malhotra, "Modulation of polarimetric coherence by ocean features," in *Geoscience and Remote Sensing Symposium, 2002. IGARSS'02. 2002 IEEE International*, vol. 1, pp. 432–434, IEEE, 2002.

List of Figures

2.1	The geometry of SAR imaging from [23]	14
2.2	The geometry of SAR imaging in the altitude ground range domain from [23]	15
2.3	The geometry of SAR imaging in the slant range azimuth domain from [23]	15
2.4	All the beam modes of Radarsat-2 from [38]	19
4.1	A photo of a natural seep in the Gulf of Mexico in image #4. Copyright OnWingsOfCare.org	26
5.1	The two first sites of the Gulf of Mexico study area. The locations where the images were acquired.	31
5.2	Third and last part from the Gulf of Mexico study area. Sargassum the point to the left and the seep the point to the right.	31
5.3	The OPV-scene in the North Sea between Norway and Scotland.	32
5.4	The SAR-subscenes that is processed in this thesis. Indication of what the images contains.	33
6.1	SAR-subscenes with indication where the pixel values for the scatter plots are taken, each box consist of 2500 pixels, except for iamage #4 which varies from 50-150	39
6.2	Segmentation of slick regions	40
7.1	Multi-polarization features calculated from the OPV-scene	50
7.2	Multi-polarization features calculated from image #1	51
7.3	Multi-polarization features calculated from image #2	52
7.4	Multi-polarization features calculated from image #3	53
7.5	Multi-polarization features calculated from image #4	54
7.6	Multi-polarization features calculated from image #5	55
7.7	Scatter plots of the entropy vs. mean radar backscatter	56
7.8	Scatter plots of the anisotropy vs. mean radar backscatter	57
7.9	Scatter plots of the real part of the co-polarization ratio vs. mean radar backscatter	58
7.10	Scatter plots of the real part of the co-polarization ratio vs. correlation magnitude	59
7.11	Histograms of the entropy from all the images	60
7.12	Histograms of the mean radar backscatter from all the images	61
7.13	Histograms of the real part of the co-polarization ratio from all the images	62
7.14	Histograms of the correlation magnitude from all the images	63
7.15	Histograms of the co-polarization ratio from all the images	64
7.16	The noise floor plotted as a function of the incidence angle. Also the mean and standard deviation of the different patches from figure 6.1 are plotted with one deviation up, and one deviation down	65
7.17	The Radarsat-2 scenes from the Gulf classified based on the mean radar backscatter feature vector	65
7.18	The Radarsat-2 scenes from the Gulf classified based the entropy feature vector	66

List of Tables

5.1	Information for all the scenes.	30
5.2	Overview of what the scenes contains.	30
7.1	Overview of all the oil-slick values. c=crude-oil, e=emulsion, p=plant-oil, ps=potential seep, s=seep, sa=sargassum	45

